

Multidimensional Modelling of Cross-Beam Energy Transfer for Direct-Drive Inertial Confinement Fusion

(Hopefully soon to be Dr.) Philip W. X. Moloney

IMPERIAL

June 2024

Submitted in partial fulfilment of the requirements for the degree of
Doctor of Philosophy of Imperial College London

Department of Physics
Imperial College London
Prince Consort Road
London SW7 2AZ

List of Acronyms

Rad-MHD Radiative-Magnetohydrodynamics

MHD Magnetohydrodynamics

Rad-Hydro Radiative-Hydrodynamics

LPIs Laser-Plasma Instabilities

CBET Cross-Beam Energy Transfer

ICF Inertial Confinement Fusion

SBS Stimulated Brillouin Scattering

SRS Stimulated Raman Scattering

TPD Two Plasmon Decay

EPW Electron Plasma Wave

LLNL Lawrence Livermore National Laboratory

IAW Ion Acoustic Wave

EPW Electron Plasma Wave

Inv-Brem Inverse-Bremsstrahlung

RTI Rayleigh–Taylor Instability

NIF National Ignition Facility

MIT Massachusetts Institute of Technology

1 Simulations of Cross-Beam Energy Transfer for Magnetised Direct-Drive

This chapter describes a set of simulations which were conducted to understand the role of Cross-Beam Energy Transfer (CBET) in magnetised, direct-drive implosions. Magnetised Inertial Confinement Fusion (ICF) is a promising route to achieving higher target gains, due to the reduction of thermal energy loss at stagnation and additional confinement of the alpha particles responsible for burn propagation. For direct-drive implosions, magnetisation can significantly alter the coronal plasma conditions, due to the introduced anisotropy of thermal transport. The Ion Acoustic Wave (IAW) dispersion relation, which mediates CBET interactions, depends upon the background plasma and therefore significantly altered temperature and density profiles could alter the action of CBET. Before the development of SOLAS, no direct-drive suitable CBET model existed, which was integrated into a Radiative-Magnetohydrodynamics (Rad-MHD) code. Therefore, the CHIMERA-SOLAS framework has enabled the effect of magnetisation on CBET to be studied for a direct-drive implosion.

The chapter begins with a review of experimental and computational work on magnetised ICF, with a particular focus on magnetised direct-drive. Work presented in this chapter focuses on the study of *exploding-pusher* experiments. These are very different implosions to the typical *central hot-spot* ignition designs, presented in previous chapters, so a short summary of exploding pushers is also provided. Simulation results are presented of 1-D and 2-D, unmagnetised exploding pushers, both with and without the effect of CBET, which demonstrate that CBET does significantly alter these implosions. This is followed by an investigation of how various extended-Magnetohydrodynamics (MHD) terms affect the implosion, including the Nernst effect, the Lorentz force and resistive diffusion of the magnetic field. Results are given of how magnetisation affects the CBET interaction and ultimately how it changes the stagnation shape of the target. The results presented, demonstrate that redistribution of deposited power due to CBET reduced the amplitude of the stagnation asymmetry, which originated from the polar beam configuration used. However, the reduction of asymmetry was consistent for different initial seed magnetic field values, and therefore CBET was not observed to be sufficiently strongly affected by magnetisation, to lead to observable signatures in experimental measurements. The chapter concludes with a summary of the work and suggestions of additional experimental configurations, which may leave a more significant signature of magnetisation altering CBET.

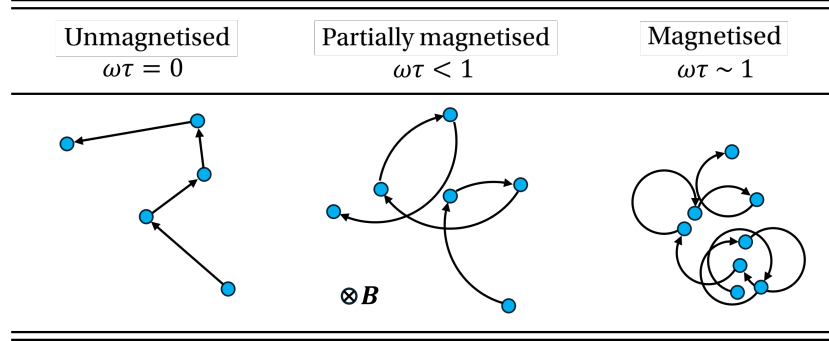


Figure 1.1: Cartoon to illustrate the effect of magnetisation on collisions, and therefore transport, of a test positive charge. Particle locations after collision are represented as blue circles and the path taken by the particle is shown by the black arrows. As the Hall parameter of the particle increases, diffusion is increasingly limited, and therefore collision transport is reduced.

1.1 Magnetised Inertial Confinement Fusion and Exploding Pushers

This chapter begins with a review of published studies of relevance to the work conducted in this chapter. Firstly, a short review of magnetised-ICF is presented, which reviews both the key concepts, existing studies and potential challenges of the design. Both work on direct- and indirect drive is summarised, alongside recent theoretical progress on understanding how magnetisation can effect Laser-Plasma Instabilities (LPIs). The exploding pusher concept is then briefly explored to aid understanding of the implosion physics, which is markedly different to conventional hot-spot ICF.

1.1.1 Potential Benefits of Target Magnetisation

Magnetisation of an ICF target has long been thought of as a potential aid to ignition [1, 2]. It is still a relevant field of study in the context of regular ignition events on the National Ignition Facility (NIF), because by relaxing the ignition threshold, magnetisation could make larger targets feasible at equivalent laser energy, and therefore lead to higher gains than unmagnetised implosions. For a central hotspot ignition targets, ignition occurs when the heat source of alpha energy deposition balances the thermal and radiative losses in the hotspot. Thermal conduction is suppressed perpendicular to magnetic field lines, therefore a magnetic field can reduce thermal losses and aid the power balance required for ignition. Fig. 1.1 demonstrates the effect of increasing magnetisation on a unit positive test charge. By constraining charged particles to orbit field lines, collisional transport terms, such as thermal conduction, are reduced perpendicular to the field direction. Fits of transport coefficients to Fokker-Planck simulations, demonstrate that in a Hydrogen plasma, thermal conductivity perpendicular to field lines κ_{\perp} , is reduced to $\sim 30\%$ of the parallel value κ_{\parallel} at Hall parameter $\omega\tau = 1$, and $\sim 1\%$ at $\omega\tau = 10$ [3]. Thus, for Hall parameters, $\omega\tau \gtrsim 10$, thermal conduction losses are almost negligible in the direction perpendicular to field lines.

Using an order of magnitude estimate for a below ignition threshold hotspot, $T_e \sim 2.5$ keV

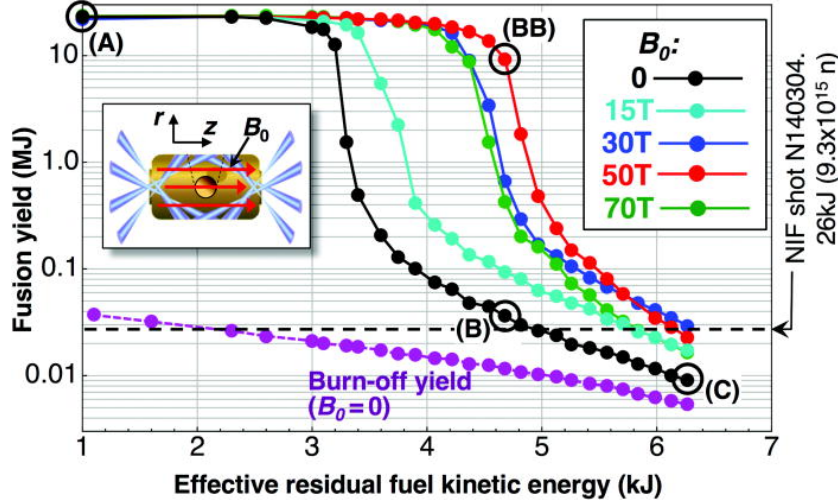


Figure 1.2: Simulated fusion yields versus effective residual fuel kinetic energy under imposed low-mode radiation flux perturbations for imposed fields in the range $B_0 = 0 \rightarrow 70$ (T). The plot demonstrates that with increasing departure from ideal compression (moving to the right on the x axis), magnetisation can enable the onset of the ignition. Reused with permission from Ref. [6].

and $\rho \sim 50 \text{ g cm}^{-3}$, a field strength $|\mathbf{B}| \sim 2.5 \text{ kT}$ is required to obtain $\omega\tau \sim 1$ [4]. This field strength cannot be produced directly, but it is possible to produce a smaller field which, assuming frozen in magnetic field and a spherical compression, is amplified by the square of the convergence,

$$|\mathbf{B}_1| = |\mathbf{B}_0| \left(\frac{R_0}{R_1} \right)^2, \quad (1.1)$$

where $|\mathbf{B}_0|$ and $|\mathbf{B}_1|$ are initial and final magnetic fields respectively and R_0 and R_1 are initial and final radii respectively. Laboratory magnetic fields can be produced from pulsed power coils with field strength $|\mathbf{B}| \sim \mathcal{O}(50)$ T [5], so even moderate convergence-ratio targets ($R_0/R_1 \sim 10$) are able to produce strongly magnetised core plasma.

Fig. ?? plots results of magnetised indirect-drive simulations, of a target on the threshold of ignition [6]. Increasing magnitude of radiation perturbation were applied to the drive (moving to the right on the x -axis), which prevent the target from achieving ignition, which is visible as the steep increase in yield, below some threshold level of perturbation. The results demonstrate that when an initial magnetic field was applied to the target, it more robustly ignited with increasing field strength due to reduced conduction losses. This simulation work, prior to the achievement of ignition on the NIF [7], motivated the development of a magnetised ICF campaign at Lawrence Livermore National Laboratory (LLNL) [8].

The CHIMERA code has been used to study a wide array of physics relevant to magnetised ICF. Simulation work has been conducted, which has shown that magnetisation can alter instability growth of magnetised laser fusion implosions. While in the deceleration phase, magnetic tension can reduce low-mode perturbation growth [9], magnetisation of directly-driven targets inhibits heatflow in the plasma corona and thus limits thermal stabilisation of short wavelength modes from laser imprint [10]. Recent work has also demonstrated that

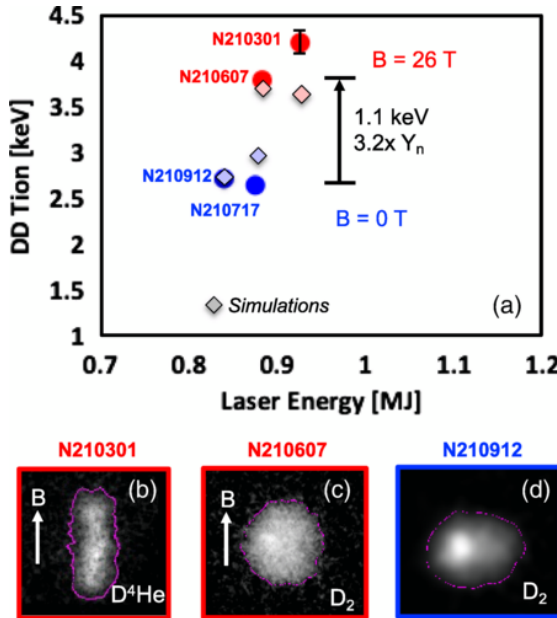


Figure 1.3: a) A 1.1 keV T_i increase was achieved by adding a 26 T B_0 field to a D_2 gas capsule implosion on the NIF. Also shown in the plot are the simulation results. b)–d) Equatorial shapes of the implosions. Reused with permission from Ref. [11].

magnetisation of high-yield, indirect-drive targets must be carefully optimised, in order to avoid significant degradation to the implosion shape, due to anisotropic thermal conduction and inhibition of burn propagation, due to α magnetisation [4].

1.1.2 Experimental Studies of Magnetised-ICF

Indirect-drive experiments have been conducted on the NIF to demonstrate the efficacy of magnetised targets, in reducing thermal conduction losses in the hotspot. Non-cryogenic, deuterium filled capsules were deployed with initial field strengths up to 26 T [11]. Results from this experimental campaign are show in Fig. 1.3.a. Fig. 1.3.b, 1.3.c and 1.3.d plot x-ray images at stagnation of different experiments, showing that a shape-tuning process had to be conducted in order to optimise the sphericity of the target, due to the field leading to anisotropic thermal conduction. The magnetised targets demonstrated significantly enhanced ion temperatures and neutron yields and work is underway to explore non-uniform field configurations to further enhance the benefits of magnetisation [12].

Magnetisation of direct-drive targets has been investigated by experiments on the OMEGA laser facility for a number of years. Initial OMEGA experiments focussed on verification of magnetic flux compression, by applying an initial seed field along the axis of a cylinder that was imploded via laser irradiation [14]. The magnetised implosions validated predictions of flux compression and demonstrated enhanced neutron yields and core ion temperatures over unmagnetised implosions. Spherical targets were subsequently fielded, which also resulted in increased stagnation temperatures and yield compared to unmagnetised targets. No noticeable degradation to the implosion shape or performance was observed in these experiments, which was assumed to be due to the high ratio of plasma pressure to magnetic

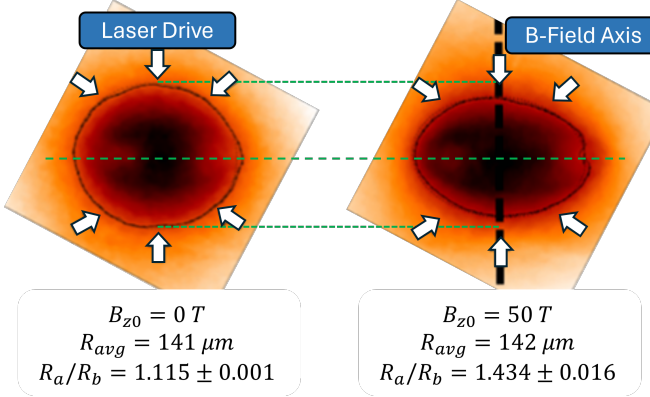


Figure 1.4: X-ray self emission images of (left) an unmagnetised and (right) a magnetised implosion. The average radius of the marked contour (corresponding to 40% of peak intensity), and the oblateness parameter R_a/R_b (ratio of major-to-minor axis) are listed below each image. The polar laser-drive is indicated by the white arrows, and the axis of the initial magnetic field by the black dashed line on the right. Applying an initial magnetic field demonstrated increased oblateness of the implosion. Adapted with permission from Ref. [13].

pressure, $\beta \gg 1$.

The most recent experimental, magnetised direct-drive work has focussed on exploring higher initial seed field values ($|\mathbf{B}_0| \sim 50$ T compared to $|\mathbf{B}_0| \sim 8$ T), to understand the saturation of performance with increasing field. A shock-driven, exploding pusher target configuration was used for these experiments, in order to create high ion temperatures and thus create a platform to study magnetised ions. Exploding pushers are significantly different implosions compared to hot-spot ignition targets discussed in previous chapters and shall be described in detail in Sec. 1.1.4. Creating these strong fields at the target necessitated reducing the radius of the equatorial field coil compared to previous experiments, and therefore a 40-beam configuration had to be used, without the 20 equatorial beams, leading to a pole heavy laser drive. The high fields of these implosions led to strongly magnetised coronal electrons, $\omega_e \tau_e \sim 50$, resulting in strongly anisotropic thermal conduction $\kappa_{\perp,e}/\kappa_{\parallel,e} \sim 10^{-4}$. This is compared to previous experiments which produced $\omega_e \tau_e \sim 1$ and therefore $\kappa_{\perp,e}/\kappa_{\parallel,e} \sim 1/3$. In direct-drive on OMEGA, laser deposition is transported to the ablation surface by electron thermal conduction, thus large electron Hall parameters led to an effective asymmetry of the implosion drive.

Fig. 1.4 shows x-ray self-emission images of an unmagnetised (left) and magnetised (right) target with an initial $|\mathbf{B}_0| = 50$ T seed field. The strongly magnetised coronal electrons led to decreased drive $\perp \hat{\mathbf{B}_0}$, markedly increasing the oblateness of the diagnostic image compared to the unmagnetised target. An ion magnetisation of $\omega_i \tau_i \sim 7$ was also reported. Previous Rad-MHD modelling of these experiments, using the CHIMERA code, did not include the effects of CBET. The development of SOLAS, and particularly the CBET model, motivated further computational study of these experiments, to explore whether CBET played a significant role in dictating the shape of these implosions. This is because CBET is known to markedly compensate global, $\ell = 1$ asymmetries [15, 16], therefore the anisotropy introduced from

magnetisation could affect the action of CBET.

1.1.3 Magnetised Laser-Plasma Instabilities

In this chapter, Sec. 1.4, aims to understand how magnetisation of a direct drive implosion anisotropically changes the hydrodynamics, and how these altered coronal plasma conditions modify the calculated CBET gains, discussed in Sec. ???. For example, magnetisation restricts thermal conduction and therefore enhances coronal electron temperatures along the initial field axis. Approximately, the fluid CBET gain, $\gamma_{ij} \propto T_e^{-1}$, therefore anisotropic changes to T_e could result in reduced CBET gains around the target and therefore change CBET scattering compared to implosions without an applied field. This modification to CBET via the altered hydrodynamic profiles is called the *indirect* effect of magnetisation on LPIs.

Magnetisation can however also *directly* modify scattering from LPIs, in a number of ways. For ICF conditions, when the field strength is sufficiently high, electron cyclotron motion can become comparable to plasma wave frequencies, and therefore alter the dispersion relation of the mediating plasma wave in LPIs. In underdense, ICF relevant plasma ($n_e \sim 10^{20} \text{ cm}^{-3}$ and $T \sim 2 \text{ keV}$), the IAW, which mediates Stimulated Brillouin Scattering (SBS) and CBET, is significantly modified when $|\mathbf{B}| \sim 100 \text{ T}$ and the Electron Plasma Wave (EPW), which mediates Stimulated Raman Scattering (SRS) and Two Plasmon Decay (TPD), when $|\mathbf{B}| \sim 1000 \text{ T}$ [17]. Additionally, the (predominantly collisionless) damping of plasma waves can also be modified, because cyclotron motion of particles can affect their trapping in plasma waves [17]. Significant theoretical progress has been made in this field in recent years by Shi et al., who derived analytic formula for 3 wave coupling in the presence of a magnetic field [18, 19]. This was challenging due to the lack of simple geometries for the interaction, when a field is applied to a plasma with an arbitrary direction.

The simulation results here neglect this direct affect of magnetisation on CBET, partially because the theory is not yet deemed to be significantly mature, to implement within a reduced, ray-based model. Coronal magnetic field strengths of $|\mathbf{B}| \lesssim 50 \text{ T}$ were observed in the underdense coronal plasma so significant modifications to the IAW dispersion relation were not expected. It is noted however, that altered damping of the waves from magnetisation may affect the results, but the focus of the study was predominantly to explore how magnetisation might indirectly affect CBET.

1.1.4 The Exploding-Pusher Configuration

Exploding-pushers are considered to be a highly reproducible platform, robust to instabilities and capable of producing large neutron yields. Although historically it had a slightly different meaning [20], the term ‘exploding pusher’ is now, typically used for low convergence, thin-shell targets [21]. When irradiated with significant intensity, frequency-tripled laser light¹, the thin shell rapidly heats and then explosively ablates, driving a strong shock

¹When frequency-tripled light is not used, suprathermal electrons, rather than ablation, is the dominant driver of the strong shock [22].

radially inward, ahead of the in-falling ablated material. This shock strongly heats the ions as it propagates through gas fill to large, fusion relevant temperatures. After rebounding from the axis, the shock recompresses the infalling exploded shell material, resulting in sufficient density for a significant number of fusion reactions.

Directly-driven exploding pusher targets have the largest direct drive fusion yields recorded on the NIF, resulting in $E_{\text{fusion}} \sim 30 \text{ kJ}$ [22]. However, they are not suitable for high gain designs, as the low areal densities of the target are not sufficient to confine α particles and thus enable burn propagation. A variety of interesting physics may be studied using the platform due to the significant ion temperatures that can be achieved, such as equilibration between electrons and ions [23]. The strong shock is also highly kinetic, and thus accurate comparison to experimentally measurable variables, such as yields and ion temperatures, is expected to be difficult for Radiative-Hydrodynamics (Rad-Hydro) codes which lack a suitable model for non-local transport, such as CHIMERA. However, much of the key dynamics and results can be studied more qualitatively. !!!!!!!!!!!!!!! - Check the above sentence and get a reference - !!!!!!!!!!!!!!!

1.2 Cross-Beam Energy Transfer in Unmagnetised Exploding Pushers

This section presents simulation results, which demonstrate the effect of CBET in exploding pushers on OMEGA. Both 1-D and 2-D CHIMERA-SOLAS simulations of 40-beam, pole-heavy drive exploding pusher experiments are presented, with a focus on how CBET acts to change the implosion. The 1-D results demonstrate that CBET significantly reduced the coupled laser energy to the implosion from ... to Simulations conducted in 2-D, with a full 3-D raytrace and CBET model, clearly demonstrated that the polar drive configuration led to an oblate implosion.

1.2.1 Simulation Configuration

The simulations conducted for this chapter aimed to study experimental configurations similar to the results from Bose *et al.*, discussed in Sec. 1.1.2 [13]. Experimental data from these magnetised exploding pushers, demonstrated a clear amplification of the mode-2 due to magnetisation, which could affect CBET scattering. The beam configuration, capsule initial conditions and pulse shape are shown in Fig. 1.5. The exact pulse shape and target specifications were from a set of follow-up experiments to Bose *et al.* and were provided by C. W. Chang and J. Frenje from Massachusetts Institute of Technology (MIT) [24]. 40 beams from the OMEGA laser, delivered a total of 17.7 kJ laser energy to a $2.5 \mu\text{m}$ thick, glass (SiO_2)² capsule, filled with room temperature and pressure D_2 . All experiments removed the 20 equatorial beams from the drive, because the presence of the field coil precluded them when an axial field was applied. Magnetic fields of strength $B_{z0} = 0, 25$ and 50 T were applied along the z-axis of the configuration.

²By ion number density, the material comprised 1/3 Si and 2/3 O.

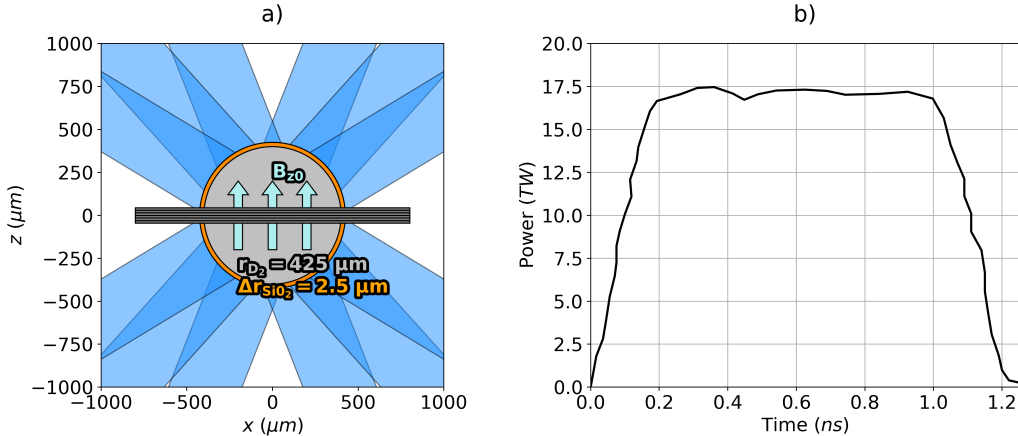


Figure 1.5: The initial conditions used for all simulations presented in this chapter. Panel a) plots the D_2 filled, glass shell capsule and direction of the initial magnetic field. An example field coil (illustrative and not included in simulations) is also shown, the presence of which necessitated the polar laser drive in experiments. Panel b) plots the laser pulse shape used, which had a total of 17.7 kJ laser energy.

An explicit $P_{1/3}$ radiation transport algorithm was used for all simulations, using tabulated opacities and emissivities from the SPK code [25]. A tabulated Sesame equation of state was used for each material [26]. The CHIMERA extended-MHD package was used, which included resistive diffusion of the magnetic field, Lorentz force of the magnetic field on the hydrodynamics, Nernst advection of the field down temperature gradients and anisotropic thermal conduction [27]. Thermal conduction was solved using a Super-time-stepping, semi-implicit algorithm [28], with flux-limited, Spitzer conductivities [29]. An electron flux limiter of $f_{lim,e} = 0.15$ was used for all simulations. Exploding pushers exhibit high coronal temperatures due to the high- Z ablator and large temperatures for the strong imploding shock, therefore simulation yields and bangtimes are highly sensitive to thermal conduction and the choice of flux limiter. Although not the focus of this work, if attempting to match simulation result to experimental yields, reducing the flux limiter value would strongly inhibit the drive and therefore reduce simulation bangtimes. In order to improve the speed of the thermal conduction algorithm, which takes small timesteps on a vacuum-plasma interface, an artificial material was placed outside the capsule, which had an enforced ionisation state of $Z = 0$. This had minimal impact on the implosion results, but significantly sped up simulation run-times. The presence of the material did create large viscous heating of the ions as the coronal plasma expanded into it which is visible in results throughout the chapter. However, this viscously heated layer was well separated from the region of interest (near critical) for the majority of the implosion and therefore did not impact upon the results.

All simulations used a spherical-polar CHIMERA mesh, with a fixed radial resolution of 0.5 μm , over the full 4π str. 1-D simulations were run from beginning to end in spherical with $r \in [0, 1400] \mu\text{m}$. 2-D, r, θ calculations assumed azimuthal symmetry of the hydrodynamics and conducted an initial ‘drive-phase’ in spherical coordinates, with $r \in [80, 1400] \mu\text{m}$, where the central cutout region was removed to avoid taking small radiation transport timesteps

due to the small cell faces close to the axis. The 2-D drive-phase grid used 120 cells in the polar direction. When the shock reached this cutout region, hydrodynamic variables were trilinearly interpolated onto a 2-D cylindrical r_{cyl}, z mesh with fixed resolution, $\Delta_{r,\text{cyl}} = \Delta_z = 1 \mu\text{m}$, and $r_{\text{cyl}} \in [0, 1200] \mu\text{m}$ and $z \in [-1200, 1200] \mu\text{m}$, for the ‘stagnation-phase’. This grid contained no singularities, unlike a 2-D spherical grid which has no cutout, and therefore excessively small radiation transport timesteps were not an issue.

All simulations used a 3-D laser ray-trace with a variety of CBET treatments. CBET was fully included for some simulations and neglected for others. Alternatively, to explore the effect that CBET *spatial redistribution* of deposited power had on implosions, some simulations were conducted without CBET, but forced to deposit the magnitude of power that was absorbed from the equivalent CBET simulation at that time. Explicitly, these simulations conducted a no-CBET ray-trace, where the power of all rays was normalised to unity. When this raytrace was complete, it read in the absorbed power from the (previously conducted) CBET simulation at that time and multiplied the (normalised) deposited power by this value. This created a hydrodynamically similar implosion to the CBET ray-trace, and via comparison of these two simulations, the impact of CBET relocation-of-deposition upon the hydrodynamics was studied. Temporally-and-spatially integrated results from all simulations are presented in Tab. 1.1 and are referred to when relevant throughout the chapter.

Several metrics have been included in the table, which are explicitly defined here. The metrics are commonly used to compare implosions in ICF, because, apart from the oblateness parameter in the last column, they can all be directly computed from experimental neutron spectra [30]. As previously stated, the bangtime is the time of peak neutron production, which for this simulation, assumes only deuterium-deuterium reactions contribute,

$$t_b = \operatorname{argmax}_t \left(\int Y_{DD}(\mathbf{x}, t) \, dV \right), \quad (1.2)$$

where Y_{DD} is the deuterium-deuterium neutron production rate, which is calculated across the CHIMERA computational grid at all locations and times throughout the simulation, using Bosch-Hale fits to the reactivity [31]. The total neutron yield is the spatially and temporally integrated neutron production,

$$Y_n = \int \int Y_{DD}(\mathbf{x}, t) \, dV \, dt. \quad (1.3)$$

The burn-width, Δ_b is the full width half maximum of the spatially integrated neutron production. One interpretation of this diagnostic, for this very two-dimensional configuration, is that a highly oblate implosion will have less temporally and spatially localised convergence. Therefore, neutron production for less symmetric implosions will likely happen over a longer timescale, because thermonuclear conditions are produced at different times in different locations. The burn-averaged ion temperature, $\langle T_i \rangle$, is defined as the ion temperature, weighted by temporally and spatially resolved neutron production,

$$\langle T_i \rangle = \frac{\int \int T_i(\mathbf{x}, t) Y_{DD}(\mathbf{x}, t) \, dV \, dt}{Y_n}, \quad (1.4)$$

Table 1.1: Results of all Simulations. In the CBET column, ‘~’ indicates CBET acted on the magnitude, but *not* spatial location, of deposition.

Run	Dim.	CBET	Note	B_{z0} (T)	t_b (ns)	$\langle T_i \rangle$ (keV)	Y_n ($\times 10^{10}$)	Δ_b (ps)	$\frac{R_{\text{equator}}}{R_{\text{pole}}} _{t=t_b}$
1	1-D	Off	-	0	0.69	14.66	11.62	87	$1.00^{+0.00}_{-0.00}$
2	1-D	On	-	0					$1.00^{+0.00}_{-0.00}$
3	2-D	Off	-	0	0.71	8.44	6.20	148	$2.96^{+0.20}_{-0.19}$
4	2-D	~	-	0	0.75	7.61	5.23	153	$3.26^{+0.25}_{-0.23}$
5	2-D	On	-	0	0.75	7.77	5.46	148	$3.23^{+0.25}_{-0.23}$
6	2-D	Off	-	25	0.74	7.26	4.73	130	$3.80^{+0.41}_{-0.33}$
7	2-D	~	-	25	0.78	6.58	4.14	125	$4.55^{+0.50}_{-0.43}$
8	2-D	On	-	25	0.78	6.72	4.44	123	$4.32^{+0.47}_{-0.41}$
9	2-D	Off	-	50	0.73	6.82	3.73	134	$4.40^{+0.43}_{-0.38}$
10	2-D	~	-	50	0.78	6.30	3.30	130	$4.92^{+0.56}_{-0.48}$
11	2-D	On	-	50	0.78	6.37	3.52	129	$4.79^{+0.55}_{-0.47}$
12	2-D	Off	No Aniso.	25	0.81	6.40	5.02	118	$3.14^{+0.68}_{-0.50}$
13	2-D	Off	No Lor.	25	0.74	7.29	4.77	131	$3.80^{+0.41}_{-0.33}$
14	2-D	Off	No Nern.	25	0.73	7.41	4.85	130	$3.74^{+0.38}_{-0.32}$
15	2-D	Off	No Resis.	25	0.73	7.07	4.59	132	$3.84^{+0.42}_{-0.33}$

It is an integrated metric, which summarises the average temperature of the regions of the implosion, which are key in producing fusion-yield. Finally, the oblateness parameter in the final column of the table, $(R_{\text{equator}}/R_{\text{pole}})|_{t=t_b}$, was obtained by fitting an ellipse (with axes orientated along $\hat{\mathbf{x}}$ and $\hat{\mathbf{z}}$), to the radius of maximum density at bangtime. The fit also returned asymmetric error bars which are presented alongside the result.

1.2.2 1-D Simulations

In order to demonstrate how CBET typically affects exploding pushers, two 1-D simulations were conducted, both with and without CBET scattering included. The no-CBET and CBET simulation results are provided in Tab. 1.1 as run 1 and run 2 respectively. Note that because the simulations were 1-D and therefore spherically symmetric, the ratio of equatorial radius to polar radius at bangtime was unity. Both of these simulations used the beam configuration from Fig. 1.5, which unlike the hydrodynamics of the simulation, is not spherically symmetric. As described in Sec. ??, a sparse 3-D SOLAS mesh was created on which to compute the correct beam interaction in 3-D. For the 1-D simulations, 23 cells were used for the underlying spherical polar mesh in the θ direction and 54 cells in the ϕ direction, which were then combined to create a semi-structured SOLAS mesh.

Absorbed laser power as a function of time from these two simulations along with streak plots of hydrodynamic variables are plotted in Fig. 1.6. The left column of panels is from

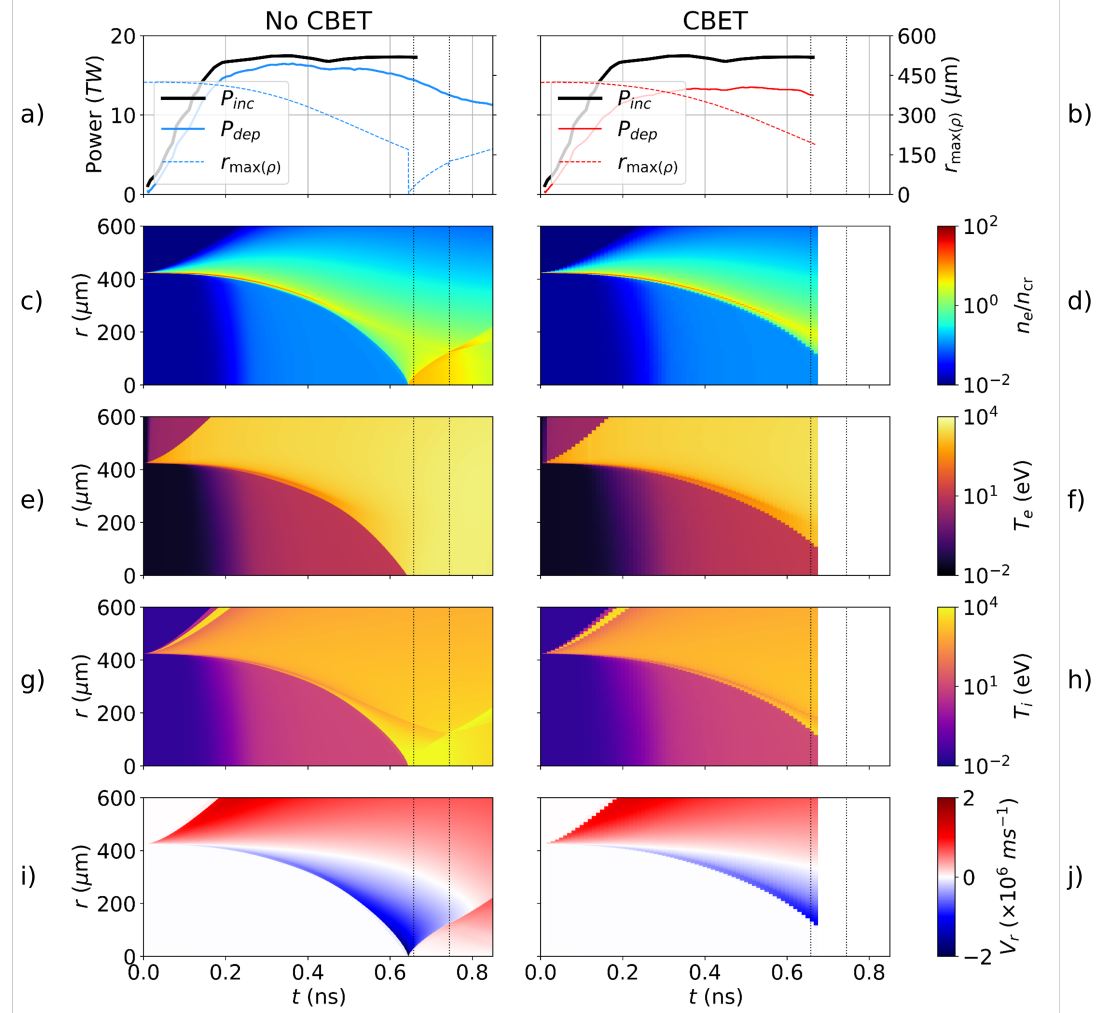


Figure 1.6: 1-D Simulation results both without (left) and with (right) CBET. The top row plots the incident and absorbed energy from the simulation on the left axis and the radius of maximum density on the right. In order, the next rows plot n_e , T_e , T_i and V_r . The full-width half-maximum times of the D₂ yield are plotted as dotted vertical black lines on all panels.

the no-CBET simulation and the right are from the CBET simulation. The top row demonstrates that CBET reduced the absorbed power by $\sim 15\%$. This reduced deposition, led to a slower and weaker shock being driven ahead of the imploding SiO₂ material, which is most clearly visible in the fourth panel, plotting T_i on a log scale. CBET reduced the speed of the shock, such that it hit the axis for the with-CBET simulation at $t \sim 0.65$ ns compared to $t \sim 0.65$ ns without CBET. Bangtime occurred for both simulations after this ‘shock-flash’, as the rebounding Deuterium fuel compressed against the in-falling shell, creating thermonuclear densities and temperatures. Note, that the effect of the fictitious, $Z = 0$ material, that was placed outside the capsule to speed up the super-time-stepping thermal conduction routine, is visible from the large T_i on the outer radius boundary of the expanding coronal plasma, which left the plot bounds at $t \sim 0.2$ ns. Simulations with vacuum outside the glass ablator initially, showed minimal difference in bangtime hydrodynamic conditions and therefore integrated diagnostics.

Compared to the streak plot of a more conventional, hot-spot ignition implosion in Fig. ??, clear differences can be seen. Firstly, the simulation presented in Fig. ?? did not include radiation transport, which is the origin of the preheat ahead of the shock³ in Fig. 1.6. Secondly, the hotspot ignition design maintained a cold dense shell throughout the implosion phase, whereas the initially thin shell of the exploding pusher simulation was approximately volumetrically heated. Therefore, relatively little mass was left in the glass shell when the re-bounding shock collided with it. Finally, the T_i increase in the exploding pusher design was predominantly from the spherical convergence of the strong shock, compared to the deceleration heating in the hotspot design, which was localised to inside the decelerating shell when it compressed on axis, at $t \sim 2.5$ ns in Fig. ???. The lack of the cold dense shell is the reason that the exploding pusher design cannot scale to high yield, as there is insufficient areal density to confine α particles and sustain a burn wave.

!!!!!!!!!!!!!! Include more stuff here about comparing the integrated diagnostics when CBET sim works! !!!!!!!

1.2.3 2-D Simulations

Simulations of this setup were also conducted in 2-D to explore how the non-uniformity of the laser-drive affected the implosion, both with and without CBET. 2-D simulations used a 3-D SOLAS mesh to resolve the beam overlap pattern, with 58 cells in the azimuthal direction. Fig. 1.7 provides plots, which illustrate the progression of the simulation during the drive-phase. The left column plots T_e , T_i and n_e from the 2-D, $B_{z0} = 0$ T simulation without CBET. Integrated results from this simulation are given in the row labelled run 3 in Tab. 1.1. The right column plots the same for the equivalent simulation, but with the effect of CBET included, which corresponds to the row labelled run 5 in Tab. 1.1. Note that the viscous ion-heating of the fictitious material placed outside the glass shell initially, is again visible as large ion temperature in the layer immediately outside the coronal plasma expansion.

Particularly at the later times plotted in Fig. 1.7, the decreased, coronal T_e of the CBET compared to the no-CBET simulation is visible. The lower T_e was because of reduced absorption, due to CBET, and led to the shock from the no-CBET simulation imploding significantly faster than the CBET shock. Thus, the no-CBET implosion was more oblate during the drive-phase, because the shock travels primarily along the \hat{z} -axis, due to the beam-geometry. However, when including CBET, the velocity of the shock was reduced more than the velocity of the imploding portion of the glass shell, *i.e.* $|V_{r,\text{shock}} - V_{r,\text{shell}}|$ was larger for the no-CBET simulation than the CBET simulation. Therefore, the no-CBET shock, after re-bounding from the axis, collided with the shell and underwent maximal neutron production at a larger radius than for the CBET result. Thus, the oblateness parameter at bangtime in Tab. 1.1, $(R_{\text{equator}}/R_{\text{pole}})|_{t=t_b}$, is significantly larger for the CBET calculation.

Both 2-D simulations exhibited substantially reduced burn-averaged ion temperatures, compared to their 1-D equivalents. This was primarily due to the strong shock travelling mainly along \hat{z} , rather than radially inward as for the 1-D calculations. Therefore, the con-

³*i.e.* The temperature increase, which is visible in T_e and T_i plots, which hit the axis at $t \sim 0.2$ ns.

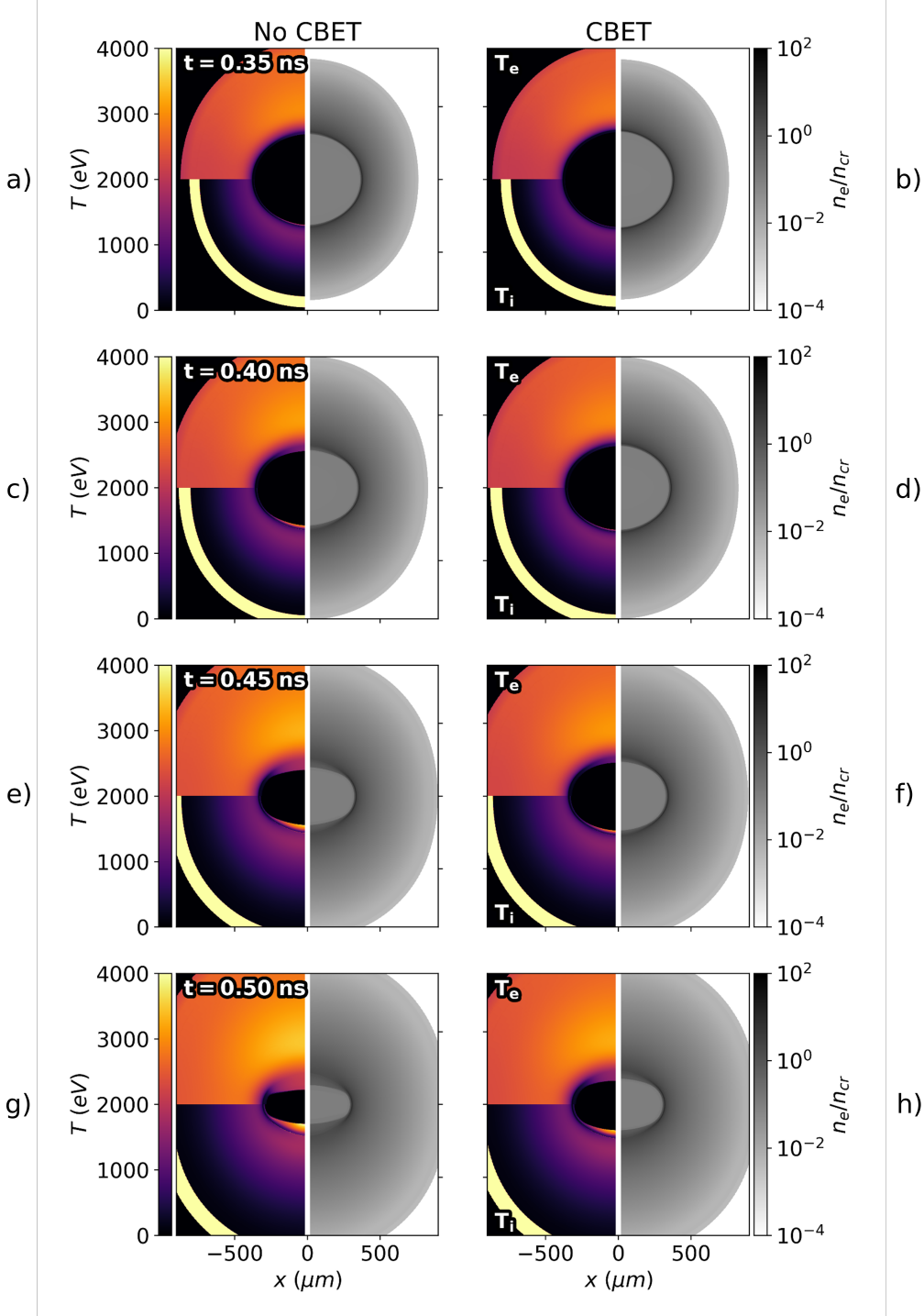


Figure 1.7: n_e (right-side), T_e (top-left-side) and T_i (bottom-left-side) plots from the 2-D, 0 T simulations without (left) and with (right) CBET at a variety of in-flight times. The decreased deposited energy due to CBET, results in lower coronal electron temperatures and therefore a slower, weaker shock being driven, which is especially evident at later times.

vergence of the shock was reduced, leading to lower temperatures, and therefore neutron yields. This interpretation is also corroborated by the increased Δ_b of all 2-D calculations compared to 1-D. The burn-width was larger, because thermonuclear conditions were pro-

duced at different times throughout the hot fuel, as the rebounding D₂ compressed against the infalling shell material, compared to the 1-D where it was spherically symmetric.

In summary of these unmagnetised implosions in 1-D and 2-D both with and without CBET, it has been shown that CBET substantially reduced the deposited power for these exploding pusher calculations. 1-D spherical calculations, which averaged the deposited power across all angles, demonstrated that this substantially reduced deposition led to a weaker shock being driven, which reduced thermonuclear yield and delayed the bangtime. When 2-D effects were included, which better reflected the geometry of the laser-drive, this resulted in an oblate implosion, which reduced the convergence of the shock, and therefore the ion temperatures. The reduced drive in the CBET calculations also slowed the shock speed more than the infalling material, so the oblateness at bangtime (when the rebounding shock collided with the in-falling material) was greater when including CBET.

1.3 Magnetisation in Exploding-Pusher Implosions

This section presents the effect that various extended-MHD terms had on the magnetised, 2-D exploding pusher simulations. Simulations were conducted with an initial field strength $B_{z0} = 25\text{T}$ and particular terms turned off, to deduce what the important physical processes were. The origin of the field structure is presented, which demonstrates that on the plasma corona, field lines are mainly radial due to the field being frozen in to highly conductive, radially outflowing plasma. Anisotropic thermal conduction in this highly magnetised coronal plasma acted to keep heat localised to the polar regions, which enhanced the drive on the pole relative to the waist. The results demonstrate that resistive diffusion and the Lorentz force have very little impact on the implosion physics, due to the bulk of the plasma being highly resistive and high- β respectively. Nernst-advection of the magnetic field acted to significantly redistribute the field in the low Hall parameter, equatorial region of the capsule, which formed a ‘divot’ in density on the capsule waist. This divot was however well separated from the region where burn was important, and thus had minimal impact on integrated neutron diagnostics.

1.3.1 In-Flight Field Structure

Initially, the development of the coronal field structure from the $B_{z0} = 25\text{T}$, no-CBET simulation, labelled as run 5 in Tab. 1.1. The top row of Fig. 1.8, plots the drive phase hydrodynamic profiles, overlaid with streamlines of the magnetic field, coloured by its magnitude, at 3 different times. Lineouts of n_e and the temperatures are plotted in the middle and bottom rows respectively, along both the polar and equatorial directions. The hot coronal plasma was highly conductive, shown explicitly in Sec. 1.3.2, and thus the field remained frozen in to the plasma. As the coronal plasma expanded outward therefore, it dragged the field lines with it, leading to $\mathbf{B} \sim \pm|\mathbf{B}|\hat{\mathbf{r}}$ in this, laser-heated region. The geometric stretching of the field lines at the target poles was less significant than at the equator, and therefore the coronal field strengths were smallest at the target equator and highest on the poles. As the target began to

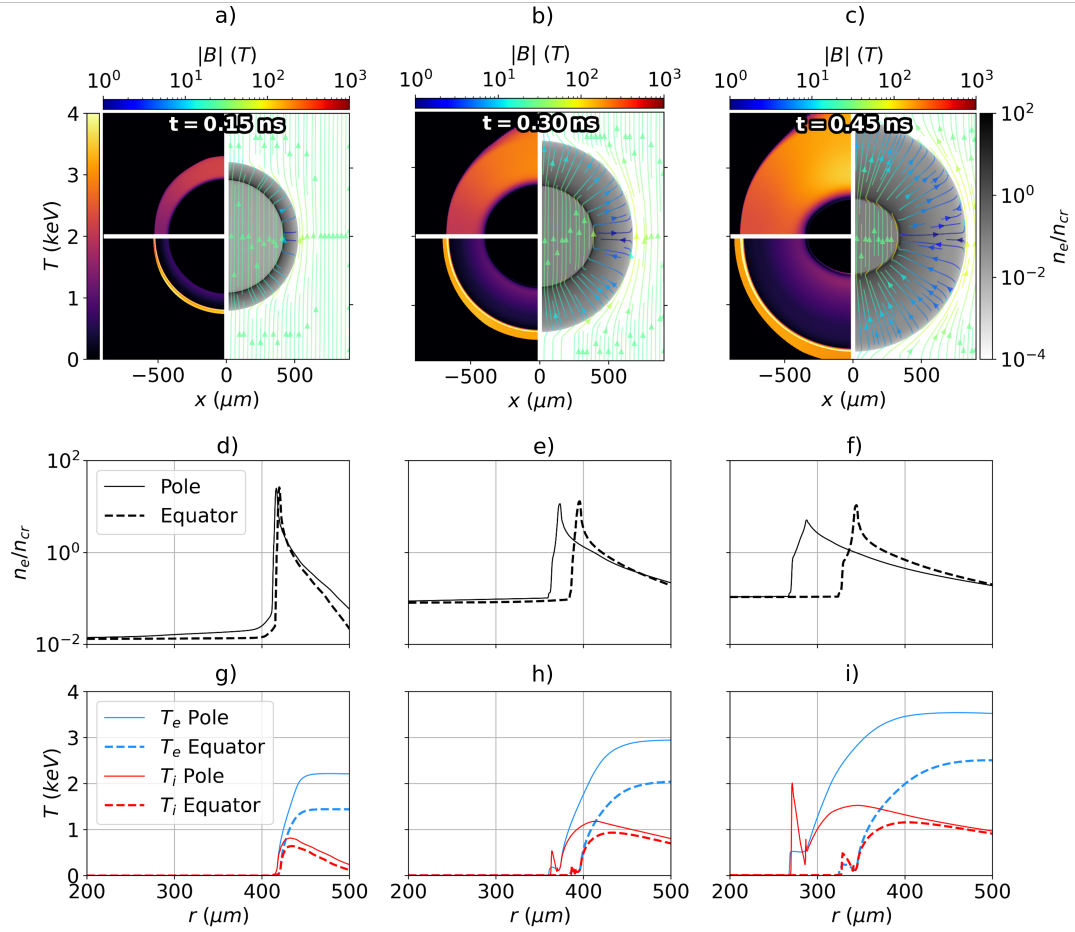


Figure 1.8: The development of the hydrodynamic variables and magnetic field structure from the $B_{z0} = 25$ T, CBET simulation. Panels a), b) and c) plot T_e (top-left), T_i (bottom-left), n_e (right) and \mathbf{B} (streamlines) at $t = 0.15, 0.30$ and 0.45 ns respectively. The approximately radially outward flowing, hot (and therefore highly conductive) ablating plasma pulled the magnetic field with it, resulting in radial \mathbf{B} field lines, which were weaker at the capsule equator. Panels d), e) and f) plot n_e lineouts along the pole ($\theta = 0^\circ$) and equator ($\theta = 90^\circ$). Panels g), h) and i) plot equivalent T_e and T_i lineouts. These all show that the increased polar temperatures, partially due to beam geometry and partially due to magnetisation, led to preferential ablation along the pole.

implode, the field compressed on the interior edge of the dense shell, resulting in non-radial field lines and an increase in field strength. This effect is most clearly visible at $t = 0.45$ ns, in Fig. 1.8.c.

The lineouts clearly demonstrate that the preferential heating of the target on the pole, led to faster ablation of the shell along this direction. This led to a much stronger shock along the pole, which is seen most clearly by the discrepancy in ion temperature between the pole and equator at $t = 0.45$ ns in Fig. 1.8.i. Increased polar electron temperature is partially due to the pole heavy drive, and also due to anisotropic thermal conduction. The field structure plotted in Fig. 1.8, inhibited equilibration of temperature via thermal conduction in the polar direction, which increased the temperature asymmetry compared to the unmagnetised

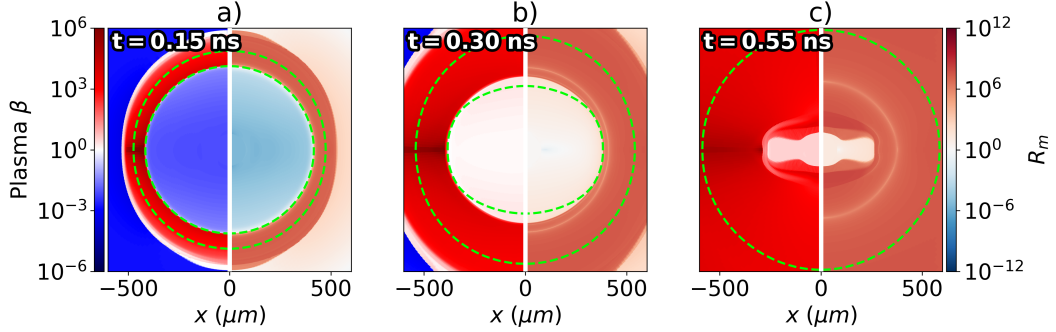


Figure 1.9: Plasma β (left-side) and Magnetic Reynolds Number, R_m , (right-side) at various in-flight times, throughout the $B_{z0} = 25$ T, no-CBET simulation. Contours of the $n_e = n_{cr}/10$ are plotted on all panels as dashed green lines to indicate the bounding region containing a significant amount plasma. Broadly, the β and R_m values are $\gg 1$ in all regions with an appreciable amount of plasma, which demonstrate that the Lorentz force and resistive diffusion respectively, should have minimal effect on the implosion dynamics.

simulation.

1.3.2 Resistive Diffusion and the Lorentz Force

As was suggested in the above Sec. 1.3.1, the coronal plasma was highly conductive for all simulations, due to its high temperatures and low densities. The right side of each panel Fig. 1.9 plots the Magnetic Reynolds Number, R_m , at three times during the implosion of the $B_{z0} = 25$ T, no-CBET simulation, labelled as run 6 in Tab. 1.1. As was stated in Sec. ??, R_m is the ratio of magnetic field advection to diffusion. Conservatively, a $1 \mu\text{m}$ length scale was used to calculate this value, which was approximately the smallest length scale observed throughout the implosion across all times. Thus, for the majority of the simulation, R_m is likely partially underestimated, because $R_m \propto L$. The green dashed lines are contours of $n_e = n_{cr}/10$, which are included to illustrate the regions of the simulation that contain the majority of the density. Although Fig. 1.9.a shows that early in the simulation, the gas fill of the capsule has a small value of R_m , and therefore resistive diffusion dominates over frozen-in flow, the dynamics of the implosion have not reached this region yet. The radiative preheat also raises the temperature, and therefore R_m value in this region, before the time plotted in Fig. 1.9.b. Therefore, the majority of the plasma has high values of R_m throughout the implosion, mainly due to the high temperatures, demonstrating that frozen-in-flow dominates over resistive diffusion. This is corroborated by comparing run 6 and run 15 in Tab. 1.1, which did not include the effects of resistive diffusion on the field transport. There is minimal difference across all metrics in this table on these two rows, which shows that the global dynamics of both simulations were very similar.

The left side of the panels in Fig. 1.9 plots the plasma β at the same times for the same simulation. As was stated in Sec. ??, this is the ratio of thermal plasma pressure to magnetic pressure and thus describes whether thermal forces or the Lorentz force, is likely to predominantly influence the plasma dynamics. Just as was seen for R_m , the value of this parameter

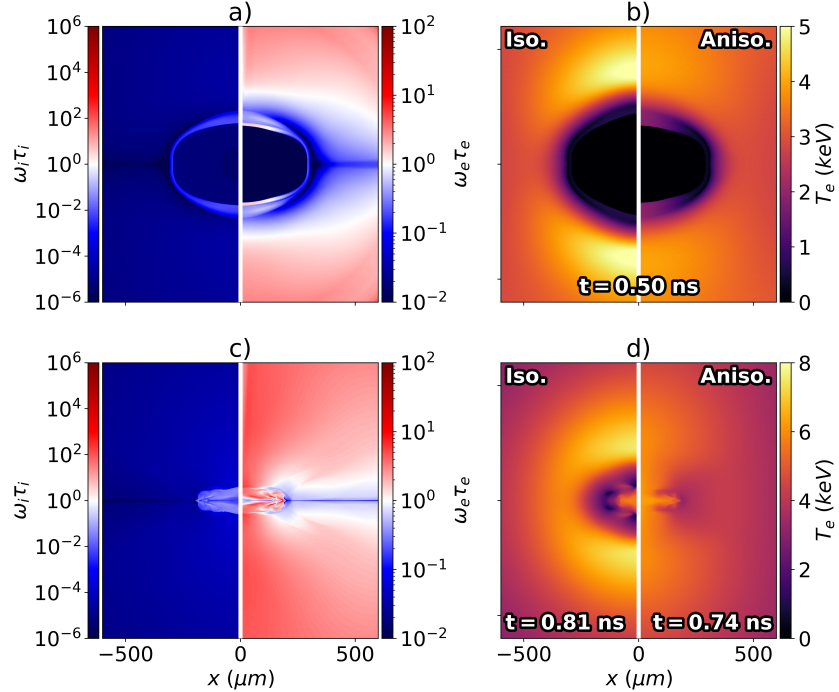


Figure 1.10: In-flight a) and bangtime c) Hall parameters, from the $B_{z0} = 25$ T, no-CBET simulation. Panel b) plots the T_e from the isotropically magnetised simulation (left-side) and anisotropic conduction simulation (right-side) in-flight. Panel d) plots the same, but at bangtime. The electron Hall parameter is > 1 at the poles due to high magnetic fields and temperatures, leading to significantly restricted thermal conduction from magnetised transport. Isotropically magnetised conduction, therefore results in a markedly different bangtime morphology, as is shown in panels b) and d). Ion hall parameters peak at bangtime, with values reaching about $\omega_i \tau_i \sim 0.1$.

is generally high in all regions with appreciable plasma density throughout the implosion, so the Lorentz force was assumed to minimally influence the plasma dynamics. An additional simulation was performed, in which the effect Lorentz force was not included on the plasma, labelled by run 13 in Tab. 1.1. Again, minimal difference was observed in the integrated metrics between this and run 6 (the comparable run, but which included the Lorentz force), which verified this analysis.

1.3.3 Anisotropic Thermal Conduction

In order to understand the effect of anisotropic thermal conduction, an additional simulation was performed, which had the same setup as the $B_{z0} = 25$ T, no-CBET, but thermal conduction was isotropically suppressed by the local magnetic field strength, regardless of its orientation. The anisotropic and isotropic simulations are labelled by run 6 and 12 respectively in Tab. 1.1. Explicitly, the parallel conductivity was forced to take the value of the perpendicular conductivity, $\kappa_{\parallel} = \kappa_{\perp}$. Comparison of this isotropically suppressed conduction simulation, with the $B_{z0} = 25$ T, no-CBET simulation, elucidated the role of anisotropic

conductivities relative to the orientation of the field. Fig. 1.10.a plots the ion (left-side) and electron (right-side) hall parameters from the $B_{z0} = 25$ T, no-CBET, anisotropic thermal conduction simulation at $t = 0.5$ ns. It can be seen that the polar region of the corona is significantly magnetised, with $1 < \omega_e \tau_e < 10$, therefore thermal conduction in this region is significantly suppressed perpendicular to the field in the anisotropic simulation, which is approximately the polar direction, as is seen in Fig. 1.8.c. Ion Hall parameters peak at values of $\omega_i \tau_i \sim 10^{-2}$, so during the in-flight, ion transport is not expected to be significantly affected by the field.

The electron temperature profiles at the same time are plotted in Fig. 1.10.b for the isotropically-magnetised conduction simulation (left-side) and anisotropic simulation (right-side). The T_e profile of the anisotropic is significantly more oblate than the isotropic simulation and the polar regions of the isotropic region are also significantly hotter. This was due to decreased transport of deposited laser energy in the isotropic to the ablation region because heat cannot freely stream radially inward along the field lines when conductivity is isotropically suppressed by the field. Isotropic magnetisation of electron transport thus leads to reduced ablation at the poles and a larger critical radius along $\pm\hat{\mathbf{z}}$, giving the implosion and shock a more round appearance.

Bangtimes temperature profiles, plotted in Fig. 1.10.d, corroborate this analysis, where the isotropic simulation has a significantly rounder shape. The oblateness parameter in Tab. 1.1, obtained by fitting an ellipse to the radius of maximum density at bangtime, also demonstrates a less oblate profile. By isotropically magnetising the conduction, $(R_{\text{equator}}/R_{\text{pole}})|_{t=t_b}$ is reduced from $3.80 \rightarrow 3.14$. The reduced ablation coupled less energy to the implosion, evident in the reduced bangtime from $t_b = 0.74 \rightarrow 0.81$ ns, going from anisotropic to isotropic thermal conduction. Yield still increased for the isotropic simulation from $4.72 \rightarrow 5.02 \times 10^{10}$, demonstrating that these integrated yield metrics are a fine balance of many factors, including coupled energy and implosion shape.

The bangtime Hall parameters are plotted in Fig. 1.10.c, which show highly magnetised electrons and moderately magnetised ions, with a maximum $\omega_i \tau_i \sim 10^{-1}$. Note that this is also for an initial field strength $B_{z0} = 25$ T simulation. For the $B_{z0} = 50$ T, with-CBET simulation, which included CBET fully and is therefore the most realistic simulation to compare with experiment at this field strength, the maximum ion Hall parameters was also $\omega_i \tau_i \sim 10^{-1}$. This is lower than the reported value of $\omega_i \tau_i \sim 1$ in the original paper [13]. However, improved sphericity of the converging shock, which could change slightly for example by changing $f_{\text{lim},e}$, would markedly boost this value. The hall parameter $\omega \tau \propto T^{3/2} |\mathbf{B}|$, so a less oblate shock would improve this by both better flux compression of the field, and higher stagnation temperatures, due to improved shock convergence.

1.3.4 The Nernst Effect

The final extended-MHD term that was independently examined was the Nernst effect. In CHIMERA, Nernst is implemented as an advection of \mathbf{B} down ∇T_e [27]. It is a collisional term, and therefore dominates in plasma with low values of $\omega_e \tau_e$. The plots of Hall parameter in

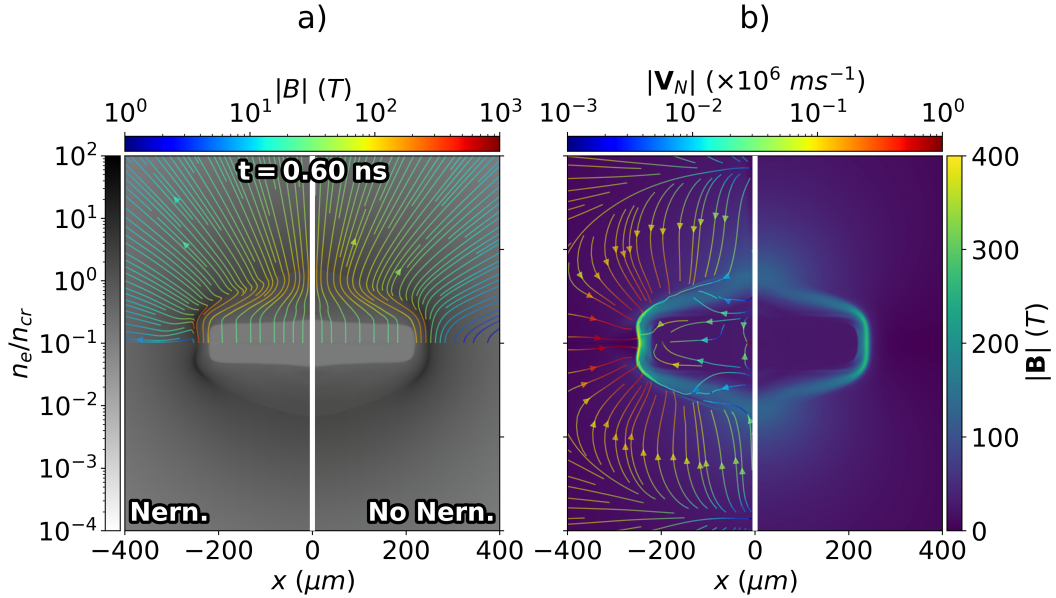


Figure 1.11: Panel a) plots in-flight electron density profiles from the $B_{z0} = 25$ T, no-CBET simulations with (left-side) and without (right-side) Nernst advection of the magnetic field. The Nernst advection velocity is also plotted for the Nernst simulation as streamlines, coloured by speed. Panel b) plots magnetic field magnitude from the Nernst (left-side) and no-Nernst (right-side) simulation along with \mathbf{B} streamlines on the top half. Advection of the field is important in the low Hall parameter equatorial region, pulling \mathbf{B} down ∇T_e , into the dense wall. Altered field at the equator impacts on the magnetised thermal conduction, which ultimately imprints on the density, as is seen in panel a).

Fig. 1.10 demonstrate that the coronal plasma has low Hall parameters in the equator, thus the Nernst effect would likely be localised to the equator of the capsule and have minimal effect on the field profiles near the poles. An additional simulation, with $B_{z0} = 25$ T, and no-CBET, was conducted without Nernst advection of magnetic field to understand its impact upon the field and plasma dynamics. The simulation without the Nernst effect is labelled in Tab. 1.1 as run 14.

Fig. 1.11.b plots the magnetic field strength equivalent simulations with Nernst (left-side) and without Nernst (right-side) at $t = 0.60$ ns. The simulation including Nernst (run 6 in Tab. 1.1), also plots the Nernst advection velocity as streamlines, coloured by the speed. The largest advection speeds are $\sim 10^6 \text{ ms}^{-1}$, which is comparable to the coronal fluid ablation speed, demonstrating that Nernst-advection is not a negligible effect in dictating the field structure. As expected, the equator of the target has the largest Nernst speeds, due to the low Hall parameter, and it acts to push field from the coronal plasma onto the interior edge of the shell. This creates a localised field ‘pile-up’ in this region for the Nernst simulation, compared to the plot on the right.

Fig. 1.11.1 plots the electron density at the same time for the Nernst (left-side) and no-Nernst (right-side) simulations alongside magnetic field streamlines from the same simulations on the top-half of the plot. The streamlines show that the Nernst effect caused the coronal field lines at the equator to be radial, by pushing B_z down the temperature gradient,

towards the shell. Here it is visible that the altered magnetic field structure has impacted on the plasma density indirectly, creating an equatorial bump in the shell, which is not present in the right-side plot without Nernst included. This bump only appeared in simulations with both Nernst and anisotropic conduction, which demonstrates that this altered field profile changed the anisotropic thermal conduction at the equator, which then impacted upon the density. The effective re-orientation of \mathbf{B} at the equator, meant that thermal conduction which transported laser energy was taken from the deposition surface to the ablation surface, experienced the higher, parallel thermal conductivity κ_{\parallel} , rather than κ_{\perp} . This locally increased the drive along $z = 0$, leading to the bump.

Comparison of run 6 (Nernst) and run 14 (no-Nernst) in Tab. 1.1, shows minimal difference on the integrated metrics, despite the altered dynamics. This is mostly because the altered profiles were localised to the equator, which was well separated from the polar region which experienced the strongest shock convergence and therefore greatest temperatures and neutron production. It is expected however, that experiments with symmetric laser illumination, and therefore a less oblate implosion, may be more influenced by the Nernst effect, because the equator of the shell would partake more in neutron production. Additionally, it is worth noting that this bump is likely to only be observed in magnetised direct-drive implosion and not indirect-drive. This is because the main action of Nernst in these simulations was to change the field in the conduction zone, which transports energy from the laser absorption region to the ablation surface for direct-drive configurations with visible wavelength light. However, for indirect drive, x-rays penetrate effectively all the way through to the ablation surface, so there is therefore no conduction zone, and the altered conduction zone field profile would have a much less significant impact on the density.

1.4 The Effect of Magnetisation on Cross-Beam Energy Transfer and Stagnation

This section presents results on how the magnetisation of the corona affects both CBET scattering and the stagnation shape of the implosion. Fig. 1.12.a plots T_e and n_e from the $B_{z0} = 0$ (left-side) and 25 T (right-side), with-CBET simulations at $t = 0.5$ ns. Fig. 1.12.b and Fig. 1.12.c plot lineouts of n_e and T_e respectively, along both the poles and equator for both simulations. While the equatorial profiles are similar, due to low Hall parameters in this region and thus minimal impact of magnetisation upon the hydrodynamics, the polar line-outs are significantly different. Magnetisation has therefore significantly amplified the $\ell = 2$ of the coronal plasma profiles which are used to calculate the CBET gain. It was therefore hypothesised that this amplified asymmetry in coronal profiles due to magnetisation, would leave a signature upon the CBET and therefore implosion dynamics, because CBET is known to interact strongly with low mode, coronal asymmetries [15].

In this chapter ‘partial-CBET’ simulations shall also be presented, for which the coupled energy was kept the same as the equivalent with-CBET simulation, *i.e.* so CBET only acted to reduce the magnitude of the deposited power, rather than redistribute it around the target. It

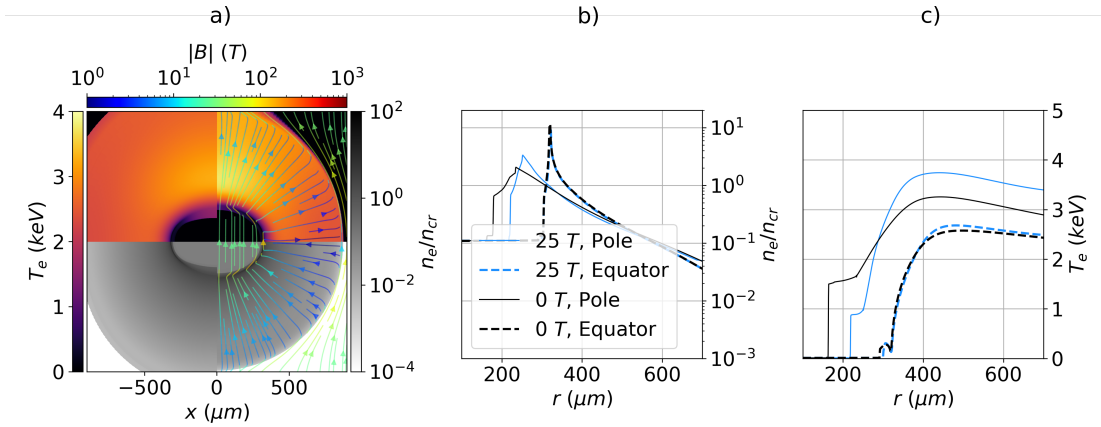


Figure 1.12: Comparison of n_e and T_e profiles from the $B_{z0} = 0$ (panel a) left-side and 25 T (panel a) right-side, with-CBET simulations, both at $t = 0.5$ ns. Panel a) also plots streamlines of \mathbf{B} for the $B_{z0} = 25$ T simulation, coloured by the field magnitude. Panels b) and c) plot n_e and T_e lineouts respectively, along both the pole and equator. It is evident from these lineouts that magnetisation anisotropically affects hydrodynamic variables, which are used to calculate the CBET gain. Therefore, it is anticipated that magnetisation could anisotropically affect the CBET scattering volume.

was hoped that, by comparison with the full-CBET simulations, this would demonstrate that CBET changed the shape of the implosion differently, for different levels of seed magnetic field. The $\ell = 2$ of the long-wavelength, density perturbation was slightly reduced by CBET, consistent with existing literature on how CBET mitigates $\ell = 1$ asymmetries [16]. Results also showed that the increasingly anisotropic coronal plasma profiles for increasing seed magnetic field strengths, did lead to changes in the CBET scattering. However, this was too small an effect to lead to experimentally observable changes in density and temperature. It is hypothesised that the polar beam geometry, shock driven characteristics of the exploding pusher implosions and high Z shell (which results in increased coronal temperatures, and therefore reduced CBET [32]), minimised the impact on hydrodynamics. Suggestions for an alternative implosion are provided, which would increase the likelihood of an experimentally observable signature.

1.4.1 Analysis and Key Definitions

Firstly, key quantities used for the analysis of this section shall be introduced. The key aim of this section was to discover if CBET acted differently in the magnetised coronal hydrodynamic profiles, compared the unmagnetised profiles. Particular focus was dedicated to discovering if this affected the implosion shape, because this shape change would not be captured by a laser-MHD model that did not have a full-CBET capability, but rather reduced the incident laser energy to compensate for CBET. Two quantities were used to understand how CBET redistributed the deposited power. The first is the ‘CBET-deficit’, which is defined as the difference in deposited power computed by a CBET and no-CBET raytrace through

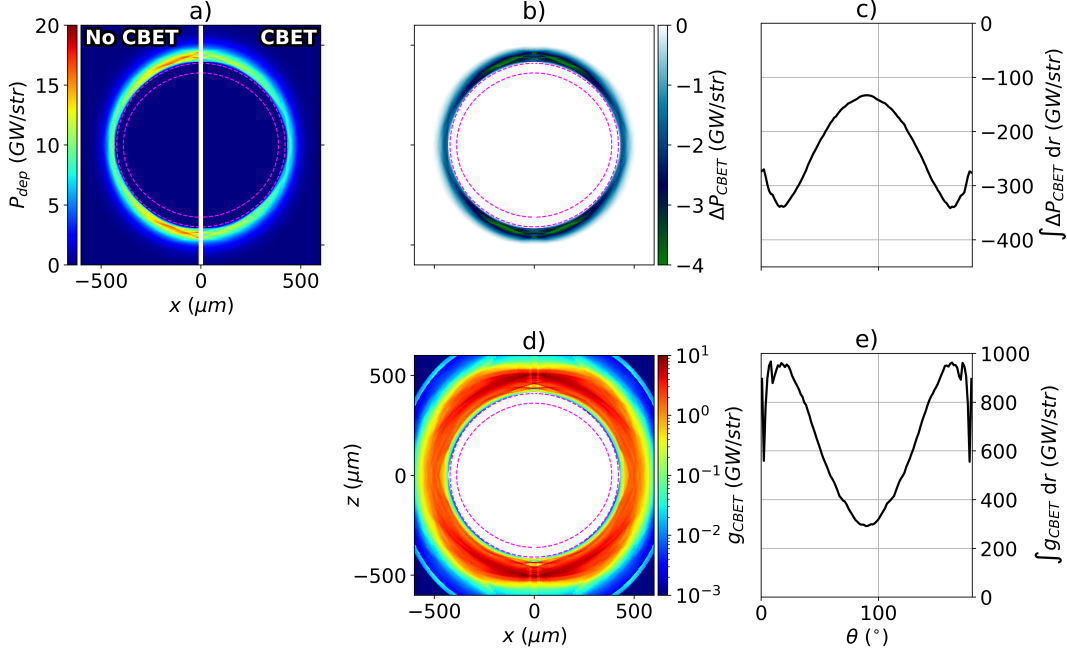


Figure 1.13: Various CBET diagnostics used in the analysis presented in this section. All plots are from the $B_{z0} = 0$ T, with-CBET simulation at $t = 0.30$ ns. Panel a) plots the instantaneous deposition with (right-side) and without (left-side) the effect of CBET. The ‘CBET-deficit’, ΔP_{CBET} , which is the no-CBET deposition, subtracted from the with-CBET deposition, is plotted in panel b). Panel c) plots the radially integrated ΔP_{CBET} , as a function of polar angle. The ‘CBET-scattering’, is plotted in panel d), and the radial integral is plotted in panel e). At this time, it is evident from panel e) that more CBET occurs at the capsule poles, resulting in a CBET-reduction of deposition near the poles, seen in panel c). The critical surface is shown in all 2-D panels by a dashed magenta line.

the *same* hydrodynamic profiles,

$$\Delta P_{\text{dep}}(\mathbf{x}, t) = P_{\text{dep}}^{\text{CBET}}(\mathbf{x}, t) - P_{\text{dep}}^{\text{no-CBET}}(\mathbf{x}, t), \quad (1.5)$$

where $P_{\text{dep}}^{\text{CBET}}$ is the deposition from the calculation including CBET and $P_{\text{dep}}^{\text{no-CBET}}(\mathbf{x}, t)$ is without CBET. As was described in Sec. ??, a CBET calculation in SOLAS always begins with a raytrace which does not include any CBET effects (the field-reconstruction raytrace), so $P_{\text{dep}}^{\text{no-CBET}}(\mathbf{x}, t)$ is the deposited power from this raytrace. $P_{\text{dep}}^{\text{CBET}}(\mathbf{x}, t)$ is the value after the pump depletion and energy conservation iterations.

Fig. 1.13.a plots the deposited power without (left-side) and with-CBET (right-side), from the $B_{z0} = 0$ T, with-CBET simulation at $t = 0.30$ ns. The corresponding CBET deficit, which is the difference between these plots, is shown in Fig. 1.13.b. Note that the value is almost all negative, because in direct-drive configurations, CBET mainly acts to reduce the intensity of light near the critical surface where Inverse-Bremsstrahlung (Inv-Brem) predominantly occurs, and therefore reduces the deposited power. There are small ($\sim 1\%$) increases in

deposition at radii outside the peak scattering surface, near Mach-1, but this is not be visible to the naked eye when the maximum colourbar scale is increased above zero. It can be seen from the CBET deficit, that at this time, CBET decreased the absorption at the poles more than at the equator of the capsule. This can be understood by considering the geometry of the pole heavy drive. The beam geometry means that the intensity is greater in the polar coronal plasma, where many beams overlap each other, therefore inbound laser sheets encounter stronger CBET resonances, as more reflected sheets are present in this region, thus their energy is depleted more than at the waist. The radial integral of the CBET deficit is plotted in Fig. 1.13.c. This conveniently illustrates the previous point, that the reduction in absorption due to CBET (at this time, of this simulation), was greater near the poles than the equator. It is also worth noting, that if CBET acted symmetrically to simply reduce the absorption, then Fig. 1.13.c would be uniform in θ . This is the case for the ‘partial-CBET’ simulations, labelled by ‘~’ under the CBET column in Tab. 1.1, where the magnitude of the power is reduced to account for CBET, but the redistribution of power is not accounted for.

The second metric that was used, is the CBET scattering, G_{CBET} , which was defined in Sec. ??, but restated here for convenience,

$$g_{\text{CBET}}(\mathbf{x}, t) = \sum_i^{\text{rays}} |\Delta P_{i,\text{CBET}}(\mathbf{x}, t)|, \quad (1.6)$$

where the time dependence has now been made explicit and $\Delta P_{i,\text{CBET}}$ is the power change of a ray due to CBET. This quantity shows where the majority of CBET power change occurred, throughout the simulation at a given time. Fig. 1.13.d plots g_{CBET} on a log scale, from the same simulation and at the same time as Fig. 1.13.a. The radial integral of this plot is shown in Fig. 1.13.e, as a function of angle. It is evident by comparison of Fig. 1.13.c and Fig. 1.13.e, that the angles of maximal CBET scattering align with the most significant deficits, and vice-versa. It should be noted that there is some noise visible in both CBET scattering plots near the poles, presumed to be due to small cells and therefore poorer ray-per-cell statistics in this region. This noise was, however, localised to a single polar-cell, and therefore not thought to have a significant impact on the overall dynamics.

1.4.2 Spatial Change of CBET and Deposition from Magnetisation

This section shall explore differences in the CBET-deficit and CBET-scattering, between magnetised and unmagnetised implosions. As was illustrated in Fig. 1.4, magnetisation significantly amplifies coronal plasma asymmetries in direct-drive implosions and thus an effect on the CBET gain calculations is expected. How changes to CBET affect the hydrodynamics and stagnation shape of the target, is discussed in the subsequent Sec. 1.4.3.

Fig. 1.14.b plots the CBET deficit as a function of time (x axis) and polar angle (y axis) for the with-CBET, $B_{z0} = 50$ T (top-half) and $B_{z0} = 0$ T (bottom-half) simulations respectively. Note that the colour scale has a maximum of zero, and is most saturated at negative values, because the radially integrated CBET-deficit was entirely negative. Lineouts in θ at three times, $t = 0.25, 0.50$ and 0.75 ns (times indicated by dashed lines on Fig. 1.14.b), are plotted in

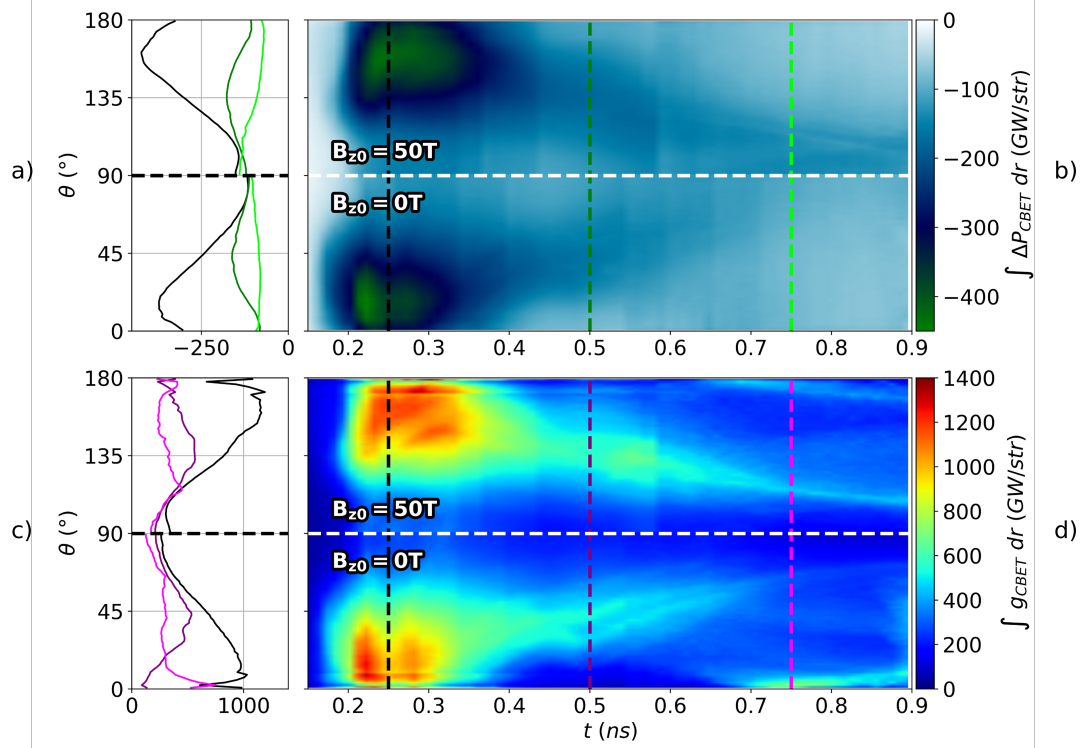


Figure 1.14: The radially integrated CBET-deficit and CBET-scattering, plotted as a function of angle and time for the $B_{z0} = 0$ and 50 T , with-CBET simulations. Panel b) plots the CBET-deficit from the 50 T (top-half) and 0 T (bottom-half) simulations. Lineouts in θ at $t = 0.25$ (black), 0.50 (dark-green) and 0.75 ns (light-green) are plotted in panel a). The same results, but for CBET-scattering are plotted in panels d) and c). It is evident from these plots that for both simulations, as time progresses and the poles of the capsule fall in faster than the equator, the region where CBET mostly occurs, shifts in angle around the capsule. Differences are visible in all plots between the $B_{z0} = 0$ and 50 T simulations, indicating that magnetisation affected CBET indirectly, via the altered hydrodynamics.

Fig. 1.14.a, where the x axis of this plot share the colour scale from Fig. 1.14.b. Broadly, both the top half and the bottom half of Fig. 1.14.b appear to be qualitatively similar. The simulation featured a large CBET-deficit of deposition near the poles between $t \sim 0.2 \rightarrow 0.3$ ns. As the implosion progressed, the asymmetry of the deficit reduced, which is visible as the reducing saturation of the plot, with increasing time. This was, however, also partially due to the lengthening of the plasma corona, which increased symmetry primarily through deposition at larger radii. Large radius deposition is less efficient at coupling to ablation, compared to if the energy were deposited close to critical, due to thermal conduction having to transport it further. An improved metric, which appropriately weights deposition by distance from the critical surface, may further elucidate the role of CBET. Both plots show behaviour, where the peak of the CBET-deficit shifted to the equator as the simulations progressed.

The CBET-scattering streak plot and lineouts in Fig. 1.14.d and 1.14.c respectively show similar behaviour. Before $t \sim 0.2$ ns, the level of CBET-scattering was low, primarily due to the low incident power, and therefore field strengths, explicitly seen by looking at the pulse

shape used in Fig. 1.5.b. Maximal scattering occurred near the poles, at early times in both the magnetised and unmagnetised simulations, which then moved more to the equator later on. The movement of the scattering and deficit to the equator was likely due to the convergence of the target. As can be seen from the time resolved n_e profiles from the with-CBET simulation in Fig. 1.7, the coronal plasma was relatively round up until $t \sim 0.35$ ns, but then began to implode more quickly along the $\pm\hat{z}$ axis than the equator. When this began to occur, the trajectory of light changed asymmetrically, resulting in a change of polar-angle where CBET predominates.

First, the expected change to the bangtime profiles from the similar, qualitative behaviour shall be described. Bangtimes for these implosions were at $t \sim 0.75$ ns, so the late time behaviour shortly before and after this, was unimportant in dictating the bangtime shapes. The most significant ΔP_{CBET} values occurred between $t \sim 0.2 \rightarrow 0.3$ ns at the poles, for both the magnetised and unmagnetised simulation. This CBET-induced power redistribution, would have reduced the strength of the shock launch along the poles, compared to the equator. Therefore, simulations with an equal magnitude of power deposition, but no spatial relocation of deposition (*i.e.* the partial-CBET simulations), were expected to exhibit a smaller $\ell = 2$ asymmetry, because CBET appeared to reduce the asymmetry of the drive.

Now, the change to the CBET deficit between the magnetised and unmagnetised simulations shall be explicitly compared. If the altered coronal plasma profiles due to magnetisation had played a dominant role in changing CBET, then the top and bottom plots would look markedly different. The similar qualitative behaviour seems to suggest therefore that this is not the dominant role in dictating implosion symmetry. Differences are observable, however, for example the magnetised simulation exhibited more CBET-scattering and a slightly larger CBET-deficit at the poles, which also lasted for a slightly longer period of time. This suggests that the shock launch in the $B_{z0} = 50$ T case would be slightly weaker than the $B_{z0} = 0$ T case. A significant reason for the small changes is that the pole-heavy drive obscures these, more subtle, changes to implosion dynamics. Explicitly, an unmagnetised, symmetric drive beam-configuration should not display an $\ell = 2$ asymmetry in either of these diagnostics, and should thus result in a symmetric bangtime profile. Changes to the shape, would therefore be much less obscured by the global asymmetry imposed by the 40-beam drive that these simulations used.

1.4.3 Stagnation Profiles

The bangtime n_e , T_e and \mathbf{B} profiles from the 2-D simulations with all magnetisations (columns) and all CBET treatments (rows) are plotted in Fig. 1.15. The top row of figures correspond to full CBET treatment and the bottom row, no effect of CBET is included. As a reminder, to conduct the partial-CBET simulations in the middle row (labelled ‘~CBET’ for shorthand), the deposited power as a function of time was loaded in from the (already completed) full-CBET simulation with the same initial B_{z0} value. No-CBET ray-traces were then conducted with incident power normalised to unity, and the deposition was multiplied by the absorbed power from the full-CBET simulation at the same time. Thus, simulations full-CBET and

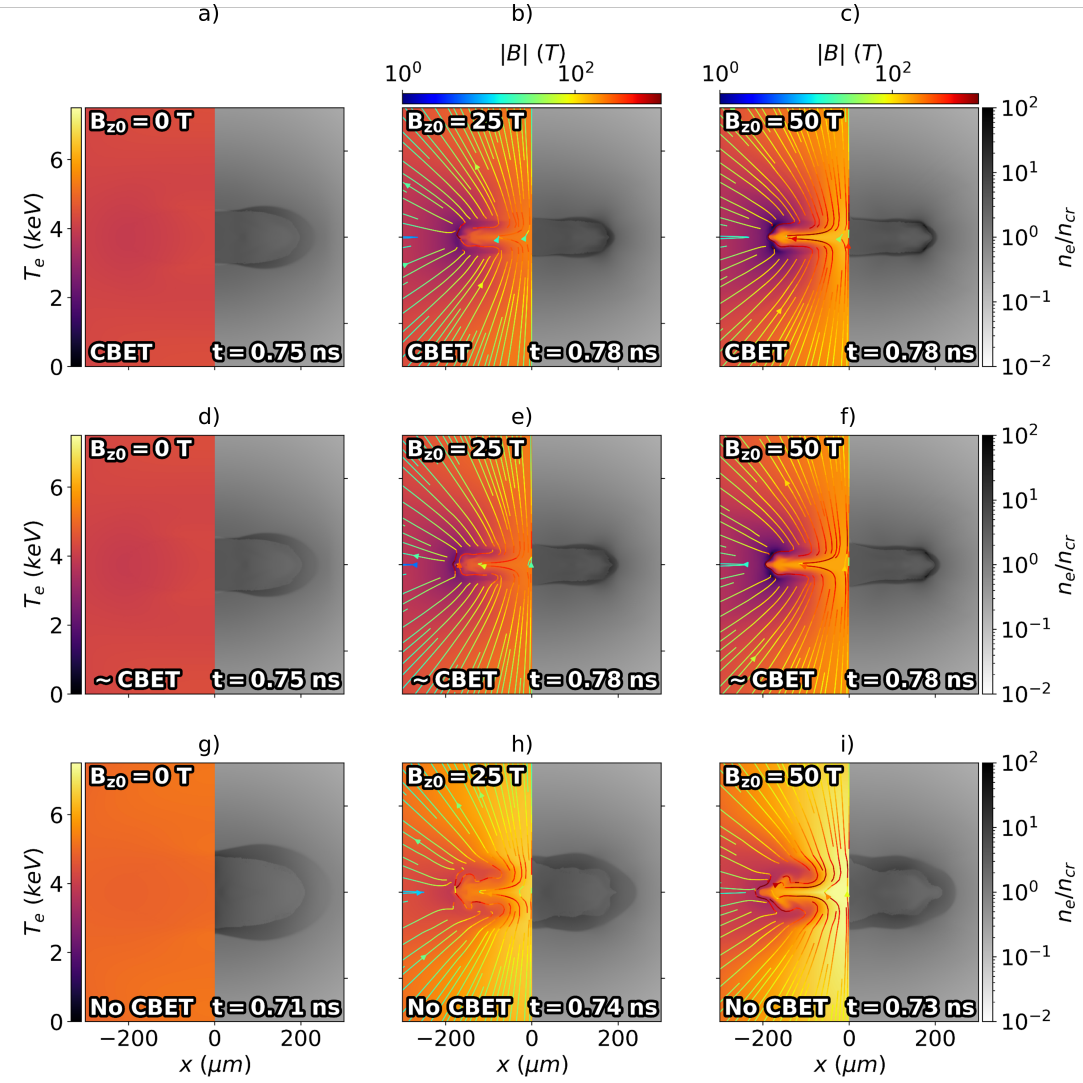


Figure 1.15: n_e , T_e and \mathbf{B} profiles from the time of peak neutron production for different initial magnetisation (columns) and CBET treatments (rows). Panels a), b) and c) are from the full CBET simulations, which show that magnetisation increases the oblateness of the stagnation profile. Panels d), e) and f) are from the simulations where only the CBET effect on the magnitude, but not spatial location, of deposition was included. These simulations have identical coupled energy to the top row, and therefore have the same bangtimes. Panels g), h) and i) are from the no-CBET simulations, which have earlier bangtimes and increased temperatures due to the higher coupled energy.

~CBET simulations with equivalent B_{z0} have identical deposition as a function of time. The only difference between them is that in the full-CBET simulations, on the top row, include redistribution of deposition around the corona.

Rows labelled run 2 → 11 in Tab. 1.1 provide the integrated metrics for each of these simulations. The first thing to note about these results, is that all implosions are oblate, *i.e.* the radius of peak density significantly larger in the equatorial direction than polar. Magnetisation also evidently flattens the implosion, regardless of CBET treatment. No-CBET simulations

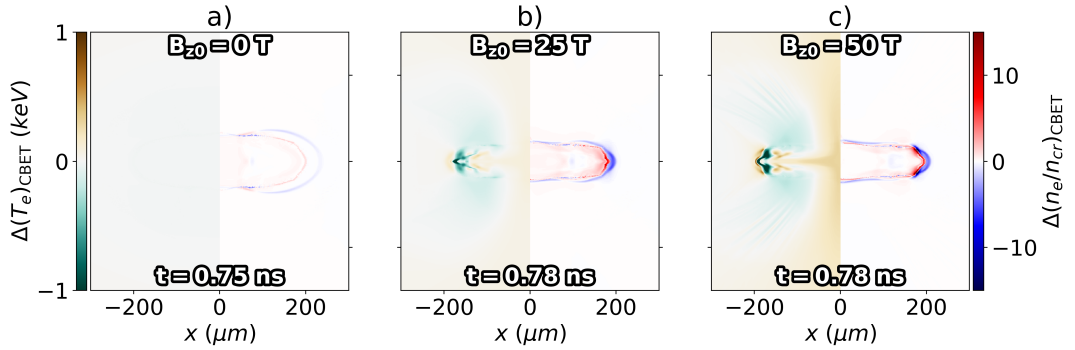


Figure 1.16: Difference in n_e and T_e bangtime profiles, between the full-CBET and CBET-magnitude a) $B_{z0} = 0$ T, b) $B_{z0} = 25$ T and c) $B_{z0} = 50$ T simulations. The difference in variable ν , is defined as $\Delta\nu = \nu_{\text{full-CB}} - \nu_{\text{partial-CB}}$, so higher colour scale values represent regions with increased ν for the full-CBET calculation. These results primarily show that CBET slightly reduces the bangtime equatorial radius, and thus reduces the oblateness, compared to simulations where the spatial redistribution of power due to CBET is neglected.

(bottom row) are also significantly less oblate than the top two rows, which both include reduced absorption due to CBET. The reason for this was described in 1.2.3. To remind the reader, it was due to the larger $|V_{r,\text{shock}} - V_{r,\text{shell}}|$ for the no-CBET simulation, compared to when CBET was included. Thus, the collision between the rebounding shock and in-falling fuel material happened at larger radii, resulting in a rounder bangtime shape.

The stagnation field structure for the magnetised simulations exhibit field lines along $z \sim 0 \mu\text{m}$ which point along $\pm\hat{x}$. This is due to the oblate structure of the initial strong shock, which moved mainly along $\pm\hat{z}$ for a wide array of x values. When the shocks from the two poles met at $z = 0 \mu\text{m}$, a thin layer was superheated to extreme temperatures (several 10keV), creating highly conductive plasma, which led to the un-shocked field along $+\hat{z}$ reorientating in the $\pm\hat{x}$ directions. The large compressed field strengths also increased the peak temperatures significantly, by insulating thermal losses. Note however, that this increase is highly anisotropic and is localised to lower density regions of the hotspot, therefore does not directly translate to increased burn-averaged temperatures in Tab. 1.1. As the bangtime temperatures and field strengths increase, the higher pressures appear to develop some form of magneto-Rayleigh–Taylor Instability (RTI) at the equator of the capsule, although the exact dynamics of this have not been studied in detail.

If CBET was anisotropically affected by magnetisation, this would result in spatial differences in deposition location, between the full CBET (top row) and CBET-on-magnitude simulations (middle row), and therefore the bangtime profiles would be different. Additionally, higher initial magnetisation increased coronal plasma anisotropy, therefore the difference between the top two rows could change as B_{z0} increased, *i.e.* from column to column. Evidently, the top rows appear very similar to each other, which illustrates that anisotropy changes to CBET from magnetised hydrodynamic profiles is a small effect compared to both the polar nature of the drive and the anisotropic drive due to magnetised transport. Small

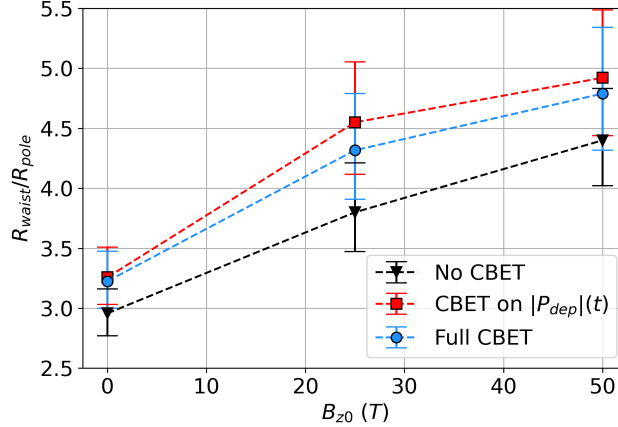


Figure 1.17: The oblateness of bangtime density profiles for different magnetisation and CBET effects. All values and errors were obtained by fitting an ellipse (with axes orientated along $\hat{\mathbf{x}}$ and $\hat{\mathbf{z}}$), to the radius of maximum density. No-CBET simulations are consistently more round, because the initial shock is stronger and therefore travels ahead of the pusher material more quickly than the CBET equivalent. Thus, after rebounding off the axis, it meets the infalling mass and produces thermonuclear conditions at a larger radius. As was seen in Fig. 1.16, throughout the entire implosion, when including the effect of CBET on spatial location of deposition, it acts to slightly move energy from the pole to the waist and thus marginally reduces oblateness of the implosion.

changes are present however, which is far more clearly displayed in Fig. 1.16. This figure plots the difference in n_e and T_e between the full-CBET (top row of 1.15) and partial-CBET (middle row of 1.15) bangtime profiles. As can be seen, differences become more significant at larger magnetisations, demonstrating that anisotropic changes of CBET scattering do impact upon the hydrodynamics. The main difference can be seen at the equator of the n_e profile, of both magnetised simulations, where the full-CBET maximum density occurs at a lower x value. Thus, CBET redistribution of deposition in magnetised coronal profiles marginally reduced the oblateness of the bangtime profile. This aligns with the expected behaviour, described at the end of Sec. 1.4.2. Restating here, the early, localised CBET-deficit should have reduced the strength of the polar shock launch compared to the equator, reducing the asymmetry of the drive and therefore the stagnation state. It was also observed that this effect seemed to become marginally more significant in magnetised coronal profiles. By comparing Fig. 1.16.a with Fig. 1.16.b and 1.16.c, the differences are slightly more significant, supporting this analysis.

The oblateness parameters from Tab. 1.1 are plotted for these implosions as a function of initial field strength. These values were obtained by fitting an ellipse to the contour of maximum density at bangtime and the fitting procedure returned asymmetric error bars which are also plotted. As was observed by examining the profiles in Fig. 1.15 directly, the no-CBET results are all significantly rounder than when the effect of CBET on deposition magnitude is included, due to the faster shock launched with greater deposited power. The partial-CBET simulations, which do not include redistribution of deposition, are all marginally more

oblate than the full-CBET simulations, with the caveat this cannot be stated conclusively, because of the error bar magnitudes. Simply stated, CBET acts to slightly reduce the oblateness of the stagnation state by effectively redistributing a small quantity of power from the poles of the capsule to the equator. There is no evidence from this plot, however, that increasing magnetisation, anisotropically alters CBET sufficiently to leave an experimental signature. If, for example, the difference between the full- and partial-CBET curves had diverged (or converged) with increasing magnetisation, this would have suggested that the increasingly anisotropic hydrodynamic profiles from magnetisation, significantly impacted upon the CBET scattering.

In retrospect, however, it was noted that the configuration used for these simulations, likely minimised any observable effect in several ways. Firstly, as discussed at the end of Sec. 1.4.2, the polar beam geometry obscured the less significant CBET anisotropy from magnetisation. Secondly, the shock driven nature of the exploding pusher configuration could have minimised experimentally observable signatures. The shape of the stagnation state is predominantly dictated by the shock launch geometry from when the shell explodes, which is mostly sensitive to the early laser-energy deposition. A more conventional, hot-spot ignition target would maintain a dense shell throughout the implosion, which would develop density modulations due to CBET-induced deposition asymmetries, as was seen in the previous chapter, for example in Fig. ???. Experimentally, a mode $\ell = 2$ is long wavelength enough to be inferred from neutron diagnostics and would thus leave an experimentally observable signature [33, 34]. Finally, higher Z ablator materials such as SiO₂, exhibit higher coronal plasma temperatures than CH, ablators, due to increased Inv-Brem. CBET in direct-drive is less significant as the coronal temperatures increase [32], therefore an experimental setup with a CH outer material, may have more CBET overall, and therefore a more easily observable change to CBET due to magnetisation.

1.5 Conclusions

1.5.1 Summary of Work

1.5.2 Future Work

Appendices

Bibliography

- [1] I.R. Lindemuth and R.C. Kirkpatrick. Parameter space for magnetized fuel targets in inertial confinement fusion. *Nuclear Fusion*, 23(3):263–284, March 1983. ISSN 0029-5515, 1741-4326. doi: 10.1088/0029-5515/23/3/001. URL <https://iopscience.iop.org/article/10.1088/0029-5515/23/3/001>. 7
- [2] R.D. Jones and W.C. Mead. The physics of burn in magnetized deuterium-tritium plasmas: spherical geometry. *Nuclear Fusion*, 26(2):127–137, February 1986. ISSN 0029-5515, 1741-4326. doi: 10.1088/0029-5515/26/2/001. URL <https://iopscience.iop.org/article/10.1088/0029-5515/26/2/001>. 7
- [3] E. M. Epperlein and M. G. Haines. Plasma transport coefficients in a magnetic field by direct numerical solution of the Fokker-Planck equation. *The Physics of Fluids*, 29(4):1029–1041, April 1986. ISSN 0031-9171. doi: 10.1063/1.865901. URL <https://pubs.aip.org/pfl/article/29/4/1029/819331/Plasma-transport-coefficients-in-a-magnetic-field>. 7
- [4] Sam Thomas Jack O'Neill. *Modelling Ignition and Burn in Pre-magnetised Inertial Confinement Fusion Experiments*. PhD thesis, Imperial College London, London, December 2023. 8, 9
- [5] G. Fiksel, A. Agliata, D. Barnak, G. Brent, P.-Y. Chang, L. Folnsbee, G. Gates, D. Hasset, D. Lonobile, J. Magoon, D. Mastrosimone, M. J. Shoup, and R. Betti. Note: Experimental platform for magnetized high-energy-density plasma studies at the omega laser facility. *Review of Scientific Instruments*, 86(1):016105, January 2015. ISSN 0034-6748, 1089-7623. doi: 10.1063/1.4905625. URL <https://pubs.aip.org/rsi/article/86/1/016105/360963>Note-Experimental-platform-for-magnetized-high>. 8
- [6] L. J. Perkins, D. D.-M Ho, B. G. Logan, G. B. Zimmerman, M. A. Rhodes, D. J. Strozzi, D. T. Blackfield, and S. A. Hawkins. The potential of imposed magnetic fields for enhancing ignition probability and fusion energy yield in indirect-drive inertial confinement fusion. *Physics of Plasmas*, 24(6):062708, June 2017. ISSN 1070-664X, 1089-7674. doi: 10.1063/1.4985150. URL <https://pubs.aip.org/pop/article/24/6/062708/108192/The-potential-of-imposed-magnetic-fields-for>. 8
- [7] A. B. Zylstra, O. A. Hurricane, D. A. Callahan, A. L. Kritcher, J. E. Ralph, H. F. Robey, J. S. Ross, C. V. Young, K. L. Baker, D. T. Casey, T. Döppner, L. Divol, M. Hohenberger, S. Le Pape, A. Pak, P. K. Patel, R. Tommasini, S. J. Ali, P. A. Amendt, L. J. Atherton, B. Bachmann, D. Bailey, L. R. Benedetti, L. Berzak Hopkins, R. Betti, S. D. Bhandarkar,

- J. Biener, R. M. Bionta, N. W. Birge, E. J. Bond, D. K. Bradley, T. Braun, T. M. Briggs, M. W. Bruhn, P. M. Celliers, B. Chang, T. Chapman, H. Chen, C. Choate, A. R. Christoperson, D. S. Clark, J. W. Crippen, E. L. Dewald, T. R. Dittrich, M. J. Edwards, W. A. Farmer, J. E. Field, D. Fittinghoff, J. Frenje, J. Gaffney, M. Gatu Johnson, S. H. Glenzer, G. P. Grim, S. Haan, K. D. Hahn, G. N. Hall, B. A. Hammel, J. Harte, E. Hartouni, J. E. Heebner, V. J. Hernandez, H. Herrmann, M. C. Herrmann, D. E. Hinkel, D. D. Ho, J. P. Holder, W. W. Hsing, H. Huang, K. D. Humbird, N. Izumi, L. C. Jarrott, J. Jeet, O. Jones, G. D. Kerbel, S. M. Kerr, S. F. Khan, J. Kilkenny, Y. Kim, H. Geppert Kleinrath, V. Geppert Kleinrath, C. Kong, J. M. Koning, J. J. Kroll, M. K. G. Kruse, B. Kustowski, O. L. Landen, S. Langer, D. Larson, N. C. Lemos, J. D. Lindl, T. Ma, M. J. MacDonald, B. J. MacGowan, A. J. Mackinnon, S. A. McLaren, A. G. MacPhee, M. M. Marinak, D. A. Mariscal, E. V. Marley, L. Masse, K. Meaney, N. B. Meezan, P. A. Michel, M. Millot, J. L. Milovich, J. D. Moody, A. S. Moore, J. W. Morton, T. Murphy, K. Newman, J.-M. G. Di Nicola, A. Nikroo, R. Nora, M. V. Patel, L. J. Pelz, J. L. Peterson, Y. Ping, B. B. Pollock, M. Ratledge, N. G. Rice, H. Rinderknecht, M. Rosen, M. S. Rubery, J. D. Salmonson, J. Sater, S. Schiaffino, D. J. Schlossberg, M. B. Schneider, C. R. Schroeder, H. A. Scott, S. M. Sepke, K. Sequoia, M. W. Sherlock, S. Shin, V. A. Smalyuk, B. K. Spears, P. T. Springer, M. Stadermann, S. Stoupin, D. J. Strozzi, L. J. Suter, C. A. Thomas, R. P. J. Town, E. R. Tubman, C. Trosseille, P. L. Volegov, C. R. Weber, K. Widmann, C. Wild, C. H. Wilde, B. M. Van Wonterghem, D. T. Woods, B. N. Woodworth, M. Yamaguchi, S. T. Yang, and G. B. Zimmerman. Burning plasma achieved in inertial fusion. *Nature*, 601(7894):542–548, January 2022. ISSN 1476-4687. doi: 10.1038/s41586-021-04281-w. URL <https://www.nature.com/articles/s41586-021-04281-w>. Publisher: Nature Publishing Group. 8
- [8] J. D. Moody, B. B. Pollock, H. Sio, D. J. Strozzi, D. D.-M. Ho, C. Walsh, G. E. Kemp, S. O. Kucheyev, B. Kozioziemski, E. G. Carroll, J. Kroll, D. K. Yanagisawa, J. Angus, S. D. Bhandarkar, J. D. Bude, L. Divol, B. Ferguson, J. Fry, L. Hagler, E. Hartouni, M. C. Herrmann, W. Hsing, D. M. Holunga, J. Javedani, A. Johnson, D. Kalantar, T. Kohut, B. G. Logan, N. Masters, A. Nikroo, N. Orsi, K. Piston, C. Provencher, A. Rowe, J. Sater, K. Skulina, W. A. Stygar, V. Tang, S. E. Winters, J. P. Chittenden, B. Appelbe, A. Boxall, A. Crilly, S. O'Neill, J. Davies, J. Peebles, and S. Fujioka. The Magnetized Indirect Drive Project on the National Ignition Facility. *Journal of Fusion Energy*, 41(1):7, June 2022. ISSN 0164-0313, 1572-9591. doi: 10.1007/s10894-022-00319-7. URL <https://link.springer.com/10.1007/s10894-022-00319-7>. 8
- [9] C. A. Walsh, K. McGlinchey, J. K. Tong, B. D. Appelbe, A. Crilly, M. F. Zhang, and J. P. Chittenden. Perturbation modifications by pre-magnetisation of inertial confinement fusion implosions. *Physics of Plasmas*, 26(2):022701, February 2019. ISSN 1070-664X, 1089-7674. doi: 10.1063/1.5085498. URL <https://pubs.aip.org/pop/article/26/2/022701/253631/Perturbation-modifications-by-pre-magnetisation-of>. 8
- [10] C.A. Walsh, A.J. Crilly, and J.P. Chittenden. Magnetized directly-driven ICF capsules:

- increased instability growth from non-uniform laser drive. *Nuclear Fusion*, 60(10):106006, October 2020. ISSN 0029-5515, 1741-4326. doi: 10.1088/1741-4326/abab52. URL <https://iopscience.iop.org/article/10.1088/1741-4326/abab52>. 8
- [11] J. D. Moody, B. B. Pollock, H. Sio, D. J. Strozzi, D. D.-M. Ho, C. A. Walsh, G. E. Kemp, B. Lahmann, S. O. Kucheyev, B. Kozioziemski, E. G. Carroll, J. Kroll, D. K. Yanagisawa, J. Angus, B. Bachmann, S. D. Bhandarkar, J. D. Bude, L. Divol, B. Ferguson, J. Fry, L. Haugler, E. Hartouni, M. C. Herrmann, W. Hsing, D. M. Holunga, N. Izumi, J. Javedani, A. Johnson, S. Khan, D. Kalantar, T. Kohut, B. G. Logan, N. Masters, A. Nikroo, N. Orsi, K. Piston, C. Provencher, A. Rowe, J. Sater, K. Skulina, W. A. Stygar, V. Tang, S. E. Winters, G. Zimmerman, P. Adrian, J. P. Chittenden, B. Appelbe, A. Boxall, A. Crilly, S. O'Neill, J. Davies, J. Peebles, and S. Fujioka. Increased Ion Temperature and Neutron Yield Observed in Magnetized Indirectly Driven D₂-Filled Capsule Implosions on the National Ignition Facility. *Physical Review Letters*, 129(19):195002, November 2022. ISSN 0031-9007, 1079-7114. doi: 10.1103/PhysRevLett.129.195002. URL <https://link.aps.org/doi/10.1103/PhysRevLett.129.195002>. 9
- [12] Chris Walsh, Dave Strozzi, John Moody, Hong Sio, Bradley Pollock, Brandon Lahmann, Blagoje Djordjevic, Alexander Lumbard, Alexander Povilus, Jeremy Chittenden, Sam O'Neill, Aidan Crilly, and Brian Appelbe. Application of Non-Uniform Magnetic Fields to Inertial Confinement Fusion Implosions. 2023:JO07.014, January 2023. URL <https://ui.adsabs.harvard.edu/abs/2023APS..DPPJ07014W>. Conference Name: APS Division of Plasma Physics Meeting Abstracts ADS Bibcode: 2023APS..DPPJ07014W. 9
- [13] A. Bose, J. Peebles, C. A. Walsh, J. A. Frenje, N. V. Kabadi, P. J. Adrian, G. D. Sutcliffe, M. Gatū Johnson, C. A. Frank, J. R. Davies, R. Betti, V. Yu. Glebov, F. J. Marshall, S. P. Regan, C. Stoeckl, E. M. Campbell, H. Sio, J. Moody, A. Crilly, B. D. Appelbe, J. P. Chittenden, S. Atzeni, F. Barbato, A. Forte, C. K. Li, F. H. Séguin, and R. D. Petrasso. Effect of Strongly Magnetized Electrons and Ions on Heat Flow and Symmetry of Inertial Fusion Implosions. *Physical Review Letters*, 128(19):195002, May 2022. ISSN 0031-9007, 1079-7114. doi: 10.1103/PhysRevLett.128.195002. URL <https://link.aps.org/doi/10.1103/PhysRevLett.128.195002>. 10, 12, 23
- [14] O. V. Gotchev, P. Y. Chang, J. P. Knauer, D. D. Meyerhofer, O. Polomarov, J. Frenje, C. K. Li, M. J.-E. Manuel, R. D. Petrasso, J. R. Rygg, F. H. Séguin, and R. Betti. Laser-Driven Magnetic-Flux Compression in High-Energy-Density Plasmas. *Physical Review Letters*, 103(21):215004, November 2009. ISSN 0031-9007, 1079-7114. doi: 10.1103/PhysRevLett.103.215004. URL <https://link.aps.org/doi/10.1103/PhysRevLett.103.215004>. 9
- [15] K. S. Anderson, C. J. Forrest, O. M. Mannion, F. J. Marshall, R. C. Shah, D. T. Michel, J. A. Marozas, P. B. Radha, D. H. Edgell, R. Epstein, V. N. Goncharov, J. P. Knauer, M. Gatū Johnson, and S. Laffite. Effect of cross-beam energy transfer on target-offset asymmetry in direct-drive inertial confinement fusion implosions.

- Physics of Plasmas*, 27(11):112713, November 2020. ISSN 1070-664X, 1089-7674. doi: 10.1063/5.0015781. URL <https://pubs.aip.org/pop/article/27/11/112713/107948/Effect-of-cross-beam-energy-transfer-on-target>. 10, 25
- [16] A. Colaïtis, I. Igumenshchev, J. Mathiaud, and V. Goncharov. Inverse ray tracing on icosahedral tetrahedron grids for non-linear laser plasma interaction coupled to 3D radiation hydrodynamics. *Journal of Computational Physics*, 443:110537, October 2021. ISSN 0021-9991. doi: 10.1016/j.jcp.2021.110537. URL <https://www.sciencedirect.com/science/article/pii/S0021999121004320>. 10, 26
- [17] Yuan Shi. Benchmarking magnetised three-wave coupling for laser backscattering: analytic solutions and kinetic simulations. *Journal of Plasma Physics*, 89(3):905890305, June 2023. ISSN 0022-3778, 1469-7807. doi: 10.1017/S0022377823000405. URL https://www.cambridge.org/core/product/identifier/S0022377823000405/type/journal_article. 11
- [18] Yuan Shi, Hong Qin, and Nathaniel J. Fisch. Three-wave scattering in magnetized plasmas: From cold fluid to quantized Lagrangian. *Physical Review E*, 96(2):023204, August 2017. ISSN 2470-0045, 2470-0053. doi: 10.1103/PhysRevE.96.023204. URL <https://link.aps.org/doi/10.1103/PhysRevE.96.023204>. 11
- [19] Yuan Shi, Hong Qin, and Nathaniel J. Fisch. Laser-plasma interactions in magnetized environment. *Physics of Plasmas*, 25(5):055706, May 2018. ISSN 1070-664X, 1089-7674. doi: 10.1063/1.5017980. URL <https://pubs.aip.org/pop/article/25/5/055706/1061011/Laser-plasma-interactions-in-magnetized>. 11
- [20] R. S. Craxton, K. S. Anderson, T. R. Boehly, V. N. Goncharov, D. R. Harding, J. P. Knauer, R. L. McCrory, P. W. McKenty, D. D. Meyerhofer, J. F. Myatt, A. J. Schmitt, J. D. Sethian, R. W. Short, S. Skupsky, W. Theobald, W. L. Kruer, K. Tanaka, R. Betti, T. J. B. Collins, J. A. Delettrez, S. X. Hu, J. A. Marozas, A. V. Maximov, D. T. Michel, P. B. Radha, S. P. Regan, T. C. Sangster, W. Seka, A. A. Solodov, J. M. Soures, C. Stoeckl, and J. D. Zuegel. Direct-drive inertial confinement fusion: A review. *Physics of Plasmas*, 22(11):110501, November 2015. ISSN 1070-664X, 1089-7674. doi: 10.1063/1.4934714. URL <https://pubs.aip.org/pop/article/22/11/110501/109006/Direct-drive-inertial-confinement-fusion-A-review>. 11
- [21] C. Leland Ellison, Heather D. Whitley, Colin R. D. Brown, Sean R. Copeland, Warren J. Garbett, Hai P. Le, Marilyn B. Schneider, Zachary B. Walters, Hui Chen, John I. Castor, R. Stephen Craxton, Maria Gatu Johnson, Emma M. Garcia, Frank R. Graziani, G. Elijah Kemp, Christine M. Krauland, Patrick W. McKenty, Brandon Lahmann, Jesse E. Pino, Michael S. Rubery, Howard A. Scott, Ronnie Shepherd, and Hong Sio. Development and modeling of a polar-direct-drive exploding pusher platform at the National Ignition Facility. *Physics of Plasmas*, 25(7):072710, July 2018. ISSN 1070-664X, 1089-7674. doi: 10.1063/1.5025724. URL <https://pubs.aip.org/pop/article/25/7/072710/319433/Development-and-modeling-of-a-polar-direct-drive>. 11

- [22] C.B. Yeamans, G.E. Kemp, Z.B. Walters, H.D. Whitley, P.W. McKenty, E.M. Garcia, Y. Yang, R.S. Craxton, and B.E. Blue. High yield polar direct drive fusion neutron sources at the National Ignition Facility. *Nuclear Fusion*, 61(4):046031, April 2021. ISSN 0029-5515, 1741-4326. doi: 10.1088/1741-4326/abe4e6. URL <https://iopscience.iop.org/article/10.1088/1741-4326/abe4e6>. 11, 12
- [23] Lorin X. Benedict, Michael P. Surh, John I. Castor, Saad A. Khairallah, Heather D. Whitley, David F. Richards, James N. Glosli, Michael S. Murillo, Christian R. Scullard, Paul E. Grabowski, David Michta, and Frank R. Graziani. Molecular dynamics simulations and generalized Lenard-Balescu calculations of electron-ion temperature equilibration in plasmas. *Physical Review E*, 86(4):046406, October 2012. ISSN 1539-3755, 1550-2376. doi: 10.1103/PhysRevE.86.046406. URL <https://link.aps.org/doi/10.1103/PhysRevE.86.046406>. 12
- [24] Cody Wu Chang and J. A. Frenje, April 2023. 12
- [25] A.J. Crilly, N.P.L. Niasse, A.R. Fraser, D.A. Chapman, K.W. McLean, S.J. Rose, and J.P. Chittenden. SpK: A fast atomic and microphysics code for the high-energy-density regime. *High Energy Density Physics*, 48:101053, September 2023. ISSN 15741818. doi: 10.1016/j.hedp.2023.101053. URL <https://linkinghub.elsevier.com/retrieve/pii/S1574181823000198>. 13
- [26] James McHardy. An introduction to the theory and use of SESAME equations of state. Technical Report LA-14503, 1487368, December 2018. URL <https://www.osti.gov/servlets/purl/1487368/>. 13
- [27] C. A. Walsh, J. P. Chittenden, D. W. Hill, and C. Ridgers. Extended-magnetohydrodynamics in under-dense plasmas. *Physics of Plasmas*, 27(2):022103, February 2020. ISSN 1070-664X, 1089-7674. doi: 10.1063/1.5124144. URL <https://pubs.aip.org/pop/article/27/2/022103/841709/Extended-magnetohydrodynamics-in-under-dense>. 13, 23
- [28] Bhargav Vaidya, Deovrat Prasad, Andrea Mignone, Prateek Sharma, and Luca Rickler. Scalable explicit implementation of anisotropic diffusion with Runge–Kutta–Legendre super-time stepping. *Monthly Notices of the Royal Astronomical Society*, 472(3):3147–3160, December 2017. ISSN 0035-8711, 1365-2966. doi: 10.1093/mnras/stx2176. URL <http://academic.oup.com/mnras/article/472/3/3147/4093858/Scalable-explicit-implementation-of-anisotropic>. 13
- [29] Lyman Spitzer and Richard Härm. Transport Phenomena in a Completely Ionized Gas. *Physical Review*, 89(5):977–981, March 1953. ISSN 0031-899X. doi: 10.1103/PhysRev.89.977. URL <https://link.aps.org/doi/10.1103/PhysRev.89.977>. 13
- [30] J A Frenje. Nuclear diagnostics for Inertial Confinement Fusion (ICF) plasmas. *Plasma Physics and Controlled Fusion*, 62(2):023001, February 2020. ISSN 0741-3335,

- 1361-6587. doi: 10.1088/1361-6587/ab5137. URL <https://iopscience.iop.org/article/10.1088/1361-6587/ab5137>. 14
- [31] H.-S Bosch and G.M Hale. Improved formulas for fusion cross-sections and thermal reactivities. *Nuclear Fusion*, 32(4):611–631, April 1992. ISSN 0029-5515. doi: 10.1088/0029-5515/32/4/I07. URL <https://iopscience.iop.org/article/10.1088/0029-5515/32/4/I07>. 14
- [32] A. Colaïtis, R. K. Follett, C. Dorrer, A. G. Seaton, D. Viala, I. Igumenshchev, D. Turnbull, V. Goncharov, and D. H. Froula. Exploration of cross-beam energy transfer mitigation constraints for designing an ignition-scale direct-drive inertial confinement fusion driver. *Physics of Plasmas*, 30(8):082701, August 2023. ISSN 1070-664X, 1089-7674. doi: 10.1063/5.0150813. URL <https://pubs.aip.org/pop/article/30/8/082701/2906541/Exploration-of-cross-beam-energy-transfer>. 26, 34
- [33] K. M. Woo, R. Betti, O. M. Mannion, C. J. Forrest, J. P. Knauer, V. N. Goncharov, P. B. Radha, D. Patel, V. Gopalaswamy, and V. Yu. Glebov. Inferring thermal ion temperature and residual kinetic energy from nuclear measurements in inertial confinement fusion implosions. *Physics of Plasmas*, 27(6):062702, June 2020. ISSN 1070-664X, 1089-7674. doi: 10.1063/1.5144460. URL <https://pubs.aip.org/pop/article/27/6/062702/1025468/Inferring-thermal-ion-temperature-and-residual>. 34
- [34] D T Casey, O L Landen, E Hartouni, R M Bionta, K D Hahn, P L Volegov, D N Fittinghoff, V Geppert-Kleinrath, C H Wilde, J L Milovich, V A Smalyuk, J E Field, O A Hurricane, A B Zylstra, A L Kritchler, D S Clark, C V Young, R C Nora, D A Callahan, B J MacGowan, D H Munro, B K Spears, J L Peterson, J A Gaffney, K D Humbird, M K G Kruse, A S Moore, D J Schlossberg, M Gatu-Johnson, and J A Frenje. Three dimensional low-mode areal-density non-uniformities in indirect-drive implosions at the National Ignition Facility. *Physics of Plasmas*, 2024. 34

Permissions